On the rectangular mesh and the decomposition of a Green's-function-based quadruple integral into elementary integrals*

Maria De Lauretis[a], Elena Haller[b], Francesca Di Murro[c], Daniele Romano[c], Giulio Antonini[c], Jonas Ekman[a], Ivana Kovačević-Badstübner[d] and Ulrike Grossner[d]

[a]Embedded Internet Systems Lab, Luleå University of Technology, Norbotten, Sweden
[b]Halmstad University, School of Information Technology, Sweden
[c]Department of Industrial and Information Engineering and Economics, Università degli Studi dell'Aquila, Abruzzo, Italy
[d]Advanced Power Semiconductor Laboratory, ETH Zurich, ETL F 28, Switzerland

ARTICLE INFO

Keywords:
Integral Equations, Discrete element method,Surface equivalence principle, Computational electromagnetics

ABSTRACT

Computational electromagnetic problems require evaluating the electric and magnetic fields of the physical object under investigation, divided into elementary cells with a mesh. The partial element equivalent circuit (PEEC) method has recently received attention from academic and industry communities because it provides a circuit representation of the electromagnetic problem. The surface formulation, known as S-PEEC, requires computing quadruple integrals for each mesh patch. Several techniques have been developed to simplify the computational complexity of quadruple integrals but limited to triangular meshes as used in well-known methods such as the Method of Moments (MoM). However, in the S-PEEC method, the mesh can be rectangular and orthogonal, and new approaches must be investigated to simplify the quadruple integrals. This work proposes a numerical approach that treats the singularity and reduces the computational complexity of one of the two quadruple integrals used in the S-PEEC method. The accuracy and computational time are tested for representative parallel and orthogonal meshes.

1. Introduction

Computational electromagnetics (CEM) problems require meshing geometrical objects by discretizing the physical geometry into elementary cells or patches. Galerkin boundary element methods (BEM), such as the Method of Moment (MoM) [1] and the Partial Element Equivalent Circuit (PEEC) method [2] require the discretization of the object and not of the surrounding medium because they are based on the integral formulation of Maxwell's equations adopting the volume or surface equivalence principles and the concept of Green's function [3]. The currents and charges are discretized by using suitable basis functions defined on spatial supports which can be either triangle cells, as in MoM [1], or parallelepipeds and rectangular cells, commonly used in the PEEC method based on the volume equivalence principle [2]. The PEEC method, based on the volume principle, results in many unknowns requiring both memory and computational power. Techniques such as the fast multipole method and multi-function techniques [4, 5], or the waveform relaxation method [6] aim to accelerate the solution of the integral equations involved. Other approaches base on model order reduction (MOR) techniques [7, 8] to reduce the complexity of the equivalent circuits and, hence, speed up the simulation. Reduced-order macro and micro modeling techniques of PEEC models have been proposed in [9, 10, 11, 12, 13].

The surface equivalence principle represents an alternative to the techniques mentioned above because it allows reducing the number of unknowns by discretizing merely the object surface, divided into elementary cells of zero thickness, that we call patches in the following. Among different types of surface formulations [14], the PEEC formulation based on the surface equivalence principle is referred to as S-PEEC [15, 16]. As in other Galerkin boundary element methods, the surface integral equations (SIEs) require the evaluation of double surface integrals, called quadruple or 4D integrals that involve the Green's function of the problem. The accuracy of the solution depends on the quality of the mesh and the accuracy in the computation of the integrals. In this work, we are interested in the second aspect only. The computational complexity of the integrals solved for the patches may cause a bottleneck in the solution due to the large computational time and memory required - the so-called "curse of dimensionality" [17, 18]. In fact, each single integral requires a certain amount of quadrature points, depending on the desired accuracy, with a rapid escalation of time and memory resources.

Moreover, the accuracy depends on the numerical evaluation of singular integrals. The kernel of the integrals is defined with Green's function, which becomes singular when the observation point and the source point coincide. This condition happens for coincident or close patches surfaces, challenging the numerical evaluation of the integrals. In this paper, we only consider integrals that show a weak singularity. The work in [19] provides a general overview of integral equations and accuracy of numerical evaluation of singular integrals in the context of the MoM. Typical techniques used for singular integrals are the singularity subtraction technique (SST), singularity cancellation methods, direct evaluation method, polar-coordinate transformation, or Duffy's transformation methods. Each method must be tailored to

*This document is the results of the research project funded by the Swedish Research Council, grant no. 2018-05252.
ORCID(s): 0000-0003-0015-0431 (M. De Lauretis)

the basis function and geometry under investigation.

Additionally, the decoupling of the charge and currents, as done in the MoM, causes singularity of the system matrix and an unstable solution at low frequency. A typical remedial technique for this problem is the loop-star decomposition [20], which allows the decomposition of the surface current into a solenoidal part and a nonsolenoidal remainder. In [21] both currents and charges are used along with both the electric and magnetic field integral equations (EFIE and MFIE, respectively) and formulate a frequency-stable integral for conductive and dielectric objects analyzed through MoM. The PEEC method inherits the beneficial effect of considering both currents and charges when it is formulated in the modified nodal analysis (MNA) form [22], as clearly shown in [23]. More recently, a rigorous *DC* solution of PEEC models has been presented in [24].

Several approaches in literature aim to manipulate the integrals so that their computation is faster and their solution is still accurate. In [25], the authors solve the surface integrals by resorting to the surface divergence theorem, together with a reordering of the integration order. However, the results are tailored for triangular surfaces, as further investigated in [18], where the authors propose a similar approach for general-case surfaces but limiting the analysis to the electrostatic case. In [26], the quadruple integrals in flat triangular patches are rewritten as the sum of regular integrals by introducing relative coordinates, followed by a generalized Duffy transform that removes the weak singularity. For triangles sharing the same face, the method admits an analytic solution. The work in [27] proposes an extension of [26], with a full numerical quadrature scheme that is not specialized for a particular integral kernel. The problem of evaluating the Green's function integrals in triangular patches is also addressed in [28], where the authors exploit a polar-coordinate transformation and a mixed analytic and numerical quadrature that mitigates the singularity and increases the accuracy of the integral computation. For the S-PEEC method with rectangular mesh, some first attempts in this direction have been made in [29, 30]. In [29], the Taylor expansion of the exponential term in the Green's function allows a complete analytic formulation of both the self-interaction and the mutual-interaction integrals. However, the accuracy depends on the Taylor expansion order, and the method suffers when used for lossy materials in the low-frequency range. The paper [30] proposes a novel semi-analytical approach for the self-interaction integrals over rectangles. The technique is based on the mathematical manipulation of the integral that is firstly converted into a two-dimensional (2D) integral, then into a one-dimensional integral by transformation into polar coordinates. This transformation not only reduces the computational complexity of the original integral, but has the advantage of handling the singularities, resulting into a stable and efficient integration.

In this work, we follow a similar approach as in [30] but extending it to the mutual-interaction integrals used in the S-PEEC method. In fact, in [30] only the local behavior of the integrals has been considered, i.e., all calculations were done for the 2D case. In the present paper, we generalize these results to the 3D case and consider different spatial configurations and aspect ratios. We provide the decomposition of the 4D integral into single or double integrals, for a rectangular and orthogonal mesh, by resorting to suitable change of variables and transformation into polar or cylindrical coordinates. We divided the analysis into two geometrical cases for rectangular patches in an orthogonal mesh: rectangles parallel and orthogonal to each other. For the parallel case, we show how to decouple the quadruple integrals into single integrals by conversion to relative coordinates, a suitable interchange of the order of integration, and a transformation into polar coordinates. For the orthogonal case, similar reasoning is used to decompose the quadruple integral into the sum of single and double integrals. The resulting integrals are solved by using the Gauss-Kronrod quadrature formula, with a transformation of weaken endpoint singularities [31, 32].

Table of notation

Bold quantities represent either field quantities or vectors.

G	Green's function	
β	phase constant (scalar)	rad/m
$\boldsymbol{r}$	radius vector of observation point (x, y, z)	
$\boldsymbol{r'}$	radius vector of source point (x', y', z')	
R	Euclidean distance defined as $\lvert\boldsymbol{r} - \boldsymbol{r'}\rvert$	m
Π'	source domain $(x', y', z') \in \Pi'$	
Π	observation domain $(x, y, z) \in \Pi$	
d_z	Π, Π'-distance, parallel case	m
ω	angular frequency	rad/s
μ	permeability	H/m
ε	permittivity	F/m
σ	conductivity	S/m
ϵ	Relative error	

2. Mathematics preliminary

The solution of an electromagnetic scattering problem commonly requires to compute vector and scalar potentials that are described in terms of Green's function. In a scattering problem, the scatter, normally a conductor, is immersed into a surrounding medium, typically free space or lossless dielectric. Similar to other EM methods for scattering problems, in the S-PEEC method the surface of the object is discretized into rectangular patches. For each patch, the surface electric and magnetic currents and charges are computed by integrating the Green's function of the problem and its curl over the pertinent domain [29]. In particular, the S-PEEC method requires the computation of the integral

$$I = \int_S \int_{S'} G(\boldsymbol{r}, \boldsymbol{r'}) dS' dS \quad \text{with } \boldsymbol{r} \in S, \boldsymbol{r'} \in S' \text{ and } S, S' \subset \mathbb{R}^3 \tag{1}$$

used in the solution of the surface Electric Field Integral Equation (s-EFIE) and Magnetic Field Integral Equation (s-MFIE) [3]. For a given source located at point $\boldsymbol{r'} = (x', y', z')$

on the elementary surface S', the Green's function G represents the spatial impulse response of the system (scatter plus surrounding) at point $\boldsymbol{r} = (x, y, z)$, located on the elementary surface S, and is defined as

$$G(\boldsymbol{r}, \boldsymbol{r'}) = \frac{\mathrm{e}^{-j\beta|\boldsymbol{r}-\boldsymbol{r'}|}}{|\boldsymbol{r}-\boldsymbol{r'}|} = \frac{\mathrm{e}^{-j\beta R}}{R} \tag{2}$$

where R is the Euclidean distance defined as $|\boldsymbol{r}-\boldsymbol{r'}|$. The β is the phase constant at an angular frequency ω, given by

$$\beta = \omega\sqrt{\mu_0\mu_r\varepsilon_0\left(\varepsilon_r + \frac{\sigma}{j\omega\varepsilon_0}\right)} \tag{3}$$

with $\mu_0, \mu_r, \varepsilon_0, \varepsilon_r$ the vacuum and relative permeability, and vacuum and relative permittivity, respectively, and σ the conductivity of the medium. The Green's function has a weak singularity because $G(\boldsymbol{r}, \boldsymbol{r'}) \sim \mathcal{O}\left(1/|\boldsymbol{r}-\boldsymbol{r'}|\right)$. Integrals in this form are often referred to as "interaction integrals" because they describe the interaction between two patch surfaces S and S'. The two surfaces are immersed in $\mathbb{R}^3$, and the integrals are quadruple integrals because they are evaluated on both surfaces. Integral (2) can be computed numerically by resorting to numerical quadrature routines that have, however, a demanding computational complexity, especially for electrically large geometries. In this work, we describe how to manipulate the 4D integrals into a sum of several elementary integrals, either single integrals or double integrals. The quadruple integrals can be decomposed into a sum of elementary integrals by conversion to relative coordinates and a suitable interchange of the order of integration. In the following, we will work on the two possible patch configurations, namely when two patch surfaces are either parallel or orthogonal to each other.

3. Decomposition of the quadruple integral - Parallel surfaces

Figure 1 shows two parallel rectangles in the 3D space:

$$\Pi = \left\{(x, y, z) \in \mathbb{R}^3 |\ x_1 \le x \le x_2,\ y_1 \le y \le y_2,\ z = z_1\right\}$$

$$\Pi' = \left\{(x', y', z') \in \mathbb{R}^3 |\ x_3 \le x' \le x_4,\ y_3 \le y' \le y_4,\ z' = z_2\right\}$$

The third component z on both surfaces is fixed, and the integral in (2) is written as

$$I_p = \int_{\Pi}\int_{\Pi'} \frac{1}{R}\mathrm{e}^{-j\beta R} dy'\, dx'\, dy\, dx \tag{4}$$

where the subscript "p" is for "parallel", and the Euclidean distance R is defined as

$$R = \sqrt{(x-x')^2 + (y-y')^2 + d_z^2} \tag{5}$$

where $d_z = |z_1 - z_2|$ is the fixed distance between the two surfaces. An important property of (4) is that the integrand merely depends on the absolute difference of the arguments, and

$$\frac{1}{R}\mathrm{e}^{-j\beta R} = f(|x-x'|, |y-y'|).$$

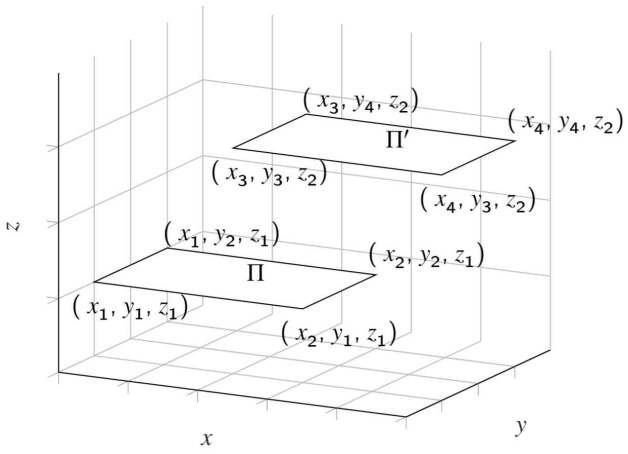

Figure 1: Two generic parallel rectangles.

In the following, we explain how to exploit this property to simplify the evaluation of the integral by changing the variables $x' \to x - x'$, $y' \to y - y'$, and by integrating explicitly over x and y. To facilitate the understanding, we start by considering the 1D-case, i.e. the integral of the form

$$I_x = \int_{x_1}^{x_2}\int_{x_3}^{x_4} f(|x-x'|)\, dx' dx\,. \tag{6}$$

Change of variable As first step, we make a change of variable $x' \to \widehat{x} = x - x'$. The integral in eq. (6) can be written as:

$$I_x = \int_{x_1}^{x_2}\int_{x-x_4}^{x-x_3} f(\widehat{x})\, d\widehat{x}\, dx\,. \tag{7}$$

The integration limits for $\widehat{x}$ depend on x, which is an unwelcome result. However, the $f(\widehat{x})$ does not formally depend on x; therefore, a proper change of order of integration solves the problem, by allowing integrating first with respect to x, and then with respect to $\widehat{x}$.

Change of the integration order We start by considering the case $|x_2 - x_1| < |x_4 - x_3|$. Note that the procedure below does not depend on mutual arrangement of Π and Π', i.e. possible spacial intersections do not affect the analysis. The understanding of the next steps is supported by the graphical representation of the integration region of integral (7) as depicted in Fig. 2. The y axis shows the different values of $\widehat{x}$ at the intersection points with the lines $x - \widehat{x}_3$ and $x - \widehat{x}_4$. Integral (7) can be evaluated as a sum of 3 integrals, for the regions R_1, R_2, and R_3 as visualized in Fig. 2, where regions R_1 and R_3 are triangles, and R_2 is a rectangle, as follows:

$$\int_{x_1}^{x_2}\int_{x-x_4}^{x-x_3} f(\widehat{x})\, d\widehat{x}\, dx = \underbrace{\int_{x_1-x_4}^{x_2-x_4}\int_{x_1}^{\widehat{x}+x_4} f(\widehat{x})\, dx\, d\widehat{x}}_{R_1}$$

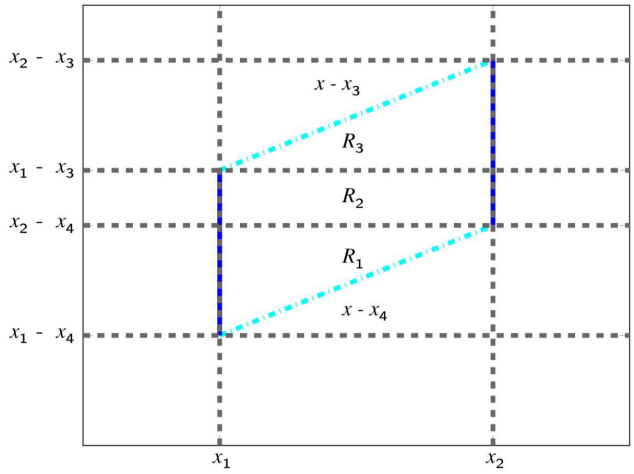

Figure 2: Integration region for the integral (7), $|x_2 - x_1| < |x_4 - x_3|$, where x is on the x-axis and $\hat{x}$ on the y-axis.

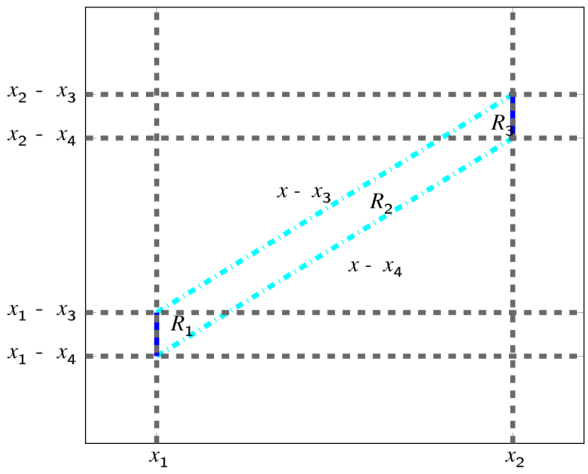

Figure 3: Integration region for the integral (7), $|x_2 - x_1| > |x_4 - x_3|$, where x is on the x-axis and $\hat{x}$ on the y-axis.

$$+ \underbrace{\int_{x_2-x_4}^{x_1-x_3}\int_{x_1}^{x_2} f(\hat{x})\,dx\,d\hat{x}}_{R_2} + \underbrace{\int_{x_1-x_3}^{x_2-x_3}\int_{\hat{x}+x_3}^{x_2} f(\hat{x})\,dx\,d\hat{x}}_{R_3}. \tag{8}$$

By integrating with respect to x, the integral (8) can be written as the sum of 3 single integrals:

$$\int_{x_1}^{x_2}\int_{x-x_4}^{x-x_3} f(\hat{x})\,d\hat{x}\,dx = \underbrace{\int_{x_1-x_4}^{x_2-x_4} f(\hat{x})(\hat{x}+x_4-x_1)\,d\hat{x}}_{R_1}$$
$$+ \underbrace{(x_2-x_1)\int_{x_2-x_4}^{x_1-x_3} f(\hat{x})\,d\hat{x}}_{R_2} + \underbrace{\int_{x_1-x_3}^{x_2-x_3} f(\hat{x})(x_2-\hat{x}-x_3)\,d\hat{x}}_{R_3}. \tag{9}$$

Remark If $|x_4 - x_3| < |x_2 - x_1|$, i.e. Π is larger than Π', the integration domain has another form, as depicted in Fig. 3. However, the integrand f depends only on the absolute value of the difference $x - x'$; this allows x-swapping $\Pi \leftrightarrow \Pi'$. Therefore, $f(x - x') = f(x' - x)$ and the case $|x_4 - x_3| < |x_2 - x_1|$ can be treated as $|x_2 - x_1| < |x_4 - x_3|$.

Carrying out the same reasoning for the y variable, the 4D integral (4) can be finally written as the sum of 9 double integrals as in eq. (10), where the constants are defined in Table 1. The evaluation of integral (10) requires the solution of the following 3 main types of double integrals:

$$I_{p1,R_{ij}} = \int_{m_1}^{m_2}\int_{n_1}^{n_2} f(\hat{x},\hat{y})\,d\hat{y}\,d\hat{x} \tag{11a}$$
for R_{ij} with $i = j = 2$,

$$I_{p2,R_{ij}} = \int_{m_1}^{m_2}\int_{n_1}^{n_2} (\hat{x}+K) f(\hat{x},\hat{y})\,d\hat{y}\,d\hat{x}, \tag{11b}$$
for R_{ij} with $i = 1,2,3$ and $j = 1,2\; i \neq j$,

$$I_{p3,R_{ij}} = \int_{m_1}^{m_2}\int_{n_1}^{n_2} (\hat{x}+K)(\hat{y}+Q) f(\hat{x},\hat{y})\,d\hat{y}\,d\hat{x}, \tag{11c}$$
for R_{ij} with $i = 1,3$ and $j = 1,3$,

where the generic integration extremes m and n are the X and the Y extremes, respectively, of the corresponding integral type in (10). The subscript R_{ij} will be omitted unless necessary.

3.1. Polar coordinates and radial behavior - parallel surfaces

The integrand (4) has radial nature and a singularity of the order $1/R$. With this respect, the transformation into polar coordinates simplifies the evaluation of (4) and also treats the singularity mentioned above. In the following, we study the transformation of the 3 integrals I_{p1}, I_{p2}, and I_{p3} into the polar coordinate system.

3.1.1. Evaluation of I_{p1}

The integral I_{p1} in (11a) can be rewritten in polar coordinates. By posing

$$\hat{x} = \rho\cos(\theta), \quad \hat{y} = \rho\sin(\theta) \tag{12}$$

with $\rho = \sqrt{\hat{x}^2+\hat{y}^2}$ and $\theta = \arctan\left(\frac{\hat{y}}{\hat{x}}\right)$, we can write

$$I_{p1} = \int_{m_1}^{m_2}\int_{n_1}^{n_2} f(\hat{x},\hat{y})\,d\hat{y}\,d\hat{x} = \int_{D_\rho}\int_{D_\theta} f(\rho)\,\rho\,d\rho\,d\theta, \tag{13}$$

where the transformed function $f(\rho)$ is

$$f(\rho) = \frac{e^{-j\beta\sqrt{\rho^2+d_z^2}}}{\sqrt{\rho^2+d_z^2}} \tag{14}$$

and D_ρ and D_θ are radial and angular domains to be specified. The aim is to integrate first with respect to θ and obtain:

$$I_{p1} = \int_{D_\rho} f(\rho)\rho d\rho \cdot \theta\Big|_{\theta_1(\rho)}^{\theta_2(\rho)} \tag{15}$$

$$\int_{\Pi}\int_{\Pi'} f(x,y,x',y')\,dx'\,dy'\,dx\,dy = \underbrace{\int_{X_1}^{X_2}\int_{Y_1}^{Y_2} f(\hat{x},\hat{y})(\hat{x}+K_1)(\hat{y}+Q_1)\,d\hat{y}\,d\hat{x}}_{R_{11}} + Q_2\underbrace{\int_{X_1}^{X_2}\int_{Y_2}^{Y_3} f(\hat{x},\hat{y})(\hat{x}+K_1)\,d\hat{y}\,d\hat{x}}_{R_{12}}$$
$$+ \underbrace{\int_{X_1}^{X_2}\int_{Y_3}^{Y_4} f(\hat{x},\hat{y})(\hat{x}+K_1)(Q_3-\hat{y})\,d\hat{y}\,d\hat{x}}_{R_{13}} + K_2\underbrace{\int_{X_2}^{X_3}\int_{Y_1}^{Y_2} f(\hat{x},\hat{y})(\hat{y}+Q_1)\,d\hat{y}\,d\hat{x}}_{R_{21}} + K_2Q_2\underbrace{\int_{X_2}^{X_3}\int_{Y_2}^{Y_3} f(\hat{x},\hat{y})\,d\hat{y}\,d\hat{x}}_{R_{22}}$$
$$+ K_2\underbrace{\int_{X_2}^{X_3}\int_{Y_3}^{Y_4} f(\hat{x},\hat{y})(Q_3-\hat{y})\,d\hat{y}\,d\hat{x}}_{R_{23}} + \underbrace{\int_{X_3}^{X_4}\int_{Y_1}^{Y_2} f(\hat{x},\hat{y})(K_3-\hat{x})(\hat{y}+Q_1)\,d\hat{y}\,d\hat{x}}_{R_{31}} + Q_2\underbrace{\int_{X_3}^{X_4}\int_{Y_2}^{Y_3} f(\hat{x},\hat{y})(K_3-\hat{x})\,d\hat{y}\,d\hat{x}}_{R_{32}}$$
$$+ \underbrace{\int_{X_3}^{X_4}\int_{Y_3}^{Y_4} f(\hat{x},\hat{y})(K_3-\hat{x})(Q_3-\hat{y})\,d\hat{y}\,d\hat{x}}_{R_{33}} \tag{10}$$

Table 1
Constants used in eq. (10) for the parallel case.

$X_1 = x_1 - x_4$	$Y_1 = y_1 - y_4$	$K_1 = x_4 - x_1$	$Q_1 = y_4 - y_1$
$X_2 = x_2 - x_4$	$Y_2 = y_2 - y_4$	$K_2 = x_2 - x_1$	$Q_2 = y_2 - y_1$
$X_3 = x_1 - x_3$	$Y_3 = y_1 - y_3$	$K_3 = x_2 - x_3$	$Q_3 = y_2 - y_3$
$X_4 = x_2 - x_3$	$Y_4 = y_2 - y_3$		

where the radial domain D_ρ does not depend on θ and is fixed. In the following, we describe how to compute the integral and define corresponding (ρ,θ)-limits of integration by mainly resorting to graphical representation. We will focus on a basic case to extend the same reasoning to all possible scenarios. The basic rectangular case has height l_1 and width l_2, with $l_1 < l_2$, as depicted in Fig. 4.

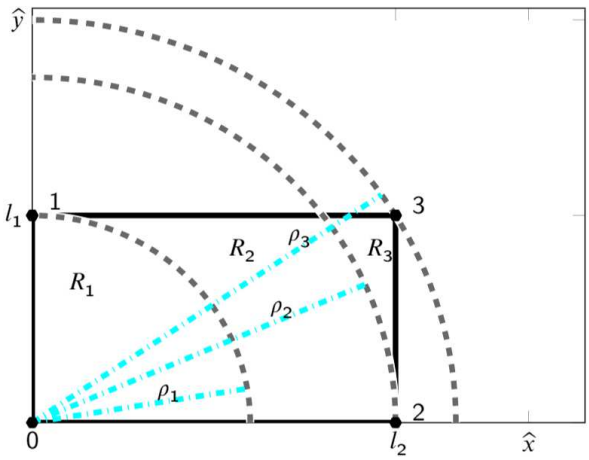

Figure 4: The basic rectangular case with $l_1 < l_2$ and polar coordinates.

Integration regions based on ρ The radial integration is the outer integration; therefore, the ρ-limits in integral (15) are expected to be fixed. In the basic rectangular case depicted in Fig. 4 we can identify 3 domains R_1, R_2 and R_3 that constitute the rectangle and allow θ-independent choice of D_ρ (corresponding radius ρ_i for $i = 1,2,3$ is showed in the figure with a dotted line). The integral (15) can be written as a sum of 3 single integrals:

$$I_{p1} = \underbrace{\int_0^{l_1} f(\rho)\,\rho\,d\rho\cdot\theta\Big|_0^{\frac{\pi}{2}}}_{R_1} + \underbrace{\int_{l_1}^{l_2} f(\rho)\,\rho\,d\rho\cdot\theta\Big|_0^{\theta_2}}_{R_2}$$
$$+ \underbrace{\int_{l_2}^{\sqrt{l_1^2+l_2^2}} f(\rho)\,\rho\,d\rho\cdot\theta\Big|_{\theta_3}^{\theta_2}}_{R_3}. \tag{16}$$

The radius ρ and angle θ for the three regions R_i of the rectangle vary in intervals as as defined in Table 2. Note that only integral I_{p1,R_1} admits a closed form solution as:

$$I_{p1,R_1} = \frac{\pi}{2}\int_0^{l_1} \frac{\rho}{\sqrt{\rho^2+d_z^2}} \mathrm{e}^{-j\beta\sqrt{\rho^2+d_z^2}} d\rho$$
$$\text{with } u \to \sqrt{\rho^2+d_z^2},\ du \to \frac{\rho}{\sqrt{\rho^2+d_z^2}} d\rho$$
$$= \frac{\pi}{2}\int_{d_z}^{\sqrt{l_1^2+d_z^2}} \mathrm{e}^{-j\beta u} du = \frac{\pi}{2}\left(\frac{j}{\beta}\mathrm{e}^{-j\beta u}\Big|_{d_z}^{\sqrt{l_1^2+d_z^2}}\right)$$
$$= j\frac{\pi}{2\beta}\left(\cos\left(\beta\sqrt{l_1^2+d_z^2}\right) - j\sin\left(\beta\sqrt{l_1^2+d_z^2}\right)\right.$$
$$\left.\cos\left(\beta d_z\right) + j\sin\left(\beta d_z\right)\right).$$

Basic rectangular case for $l_1 > l_2$ in I_{p1} Similarly as it was done for the surfaces Π and Π' when Π was larger than Π', this case can be easily handled as the basic rectangle with $l_1 < l_2$ by exchanging the x and y coordinates.

Table 2
Radial distances d and angles θ of the three regions R_i for the basic rectangular case in Fig. 4.

$\rho_1(\hat{x})$	$\hat{x} \in [0, l_1]$	$\theta \in \left[0, \pi/2\right]$
$\rho_2(\hat{x})$	$\hat{x} \in [l_1, l_2]$	$\theta \in \left[0, \theta_2\right]$, $\theta_2 = \arctan\left(\frac{l_1}{\sqrt{\rho^2 - l_1^2}}\right)$
$\rho_3(\hat{x})$	$\hat{x} \in \left[l_2, \sqrt{l_1^2 + l_2^2}\right]$	$\theta \in \left[\theta_3, \theta_2\right]$, $\theta_3 = \arctan\left(\frac{\sqrt{\rho^2 - l_2^2}}{l_2}\right)$

3.1.2. *Generalization of the integral I_{p1} in cylindrical coordinates*

The integral (16) is valid for a rectangle with the lower left corner in $(0, 0)$, lying in the first quadrant, and $l_1 < l_2$. In this section, we show how to generalize it for all possible configurations, under the assumption that $l_1 < l_2$, because the case of $l_1 > l_2$ can be handled how explained in the previous section.

Rectangle placed in the first quadrant We recall that our goal is to write the general integral (11a), hereby reported for convenience

$$I_{p1} = \int_{m_1}^{m_2} \int_{n_1}^{n_2} f(\hat{x}, \hat{y})\, d\hat{y}\, d\hat{x} \tag{17}$$

in polar coordinates, by using the formula (16). We consider a rectangular surface Π placed in the first quadrant and whose lower-left corner is in the generic point (m_1, n_1), and whose higher-right corner is in the generic point (m_2, n_2). The surface lies in the first quadrant, therefore:

$$m_1 > 0\,, \quad m_2 > 0\,, \quad n_1 > 0\,, \quad n_2 > 0\,. \tag{18}$$

As mentioned, we can focus on rectangles whose height is less the width ($l_1 > l_2$ in the previous section), therefore we can safely assume that $n_2 - n_1 < m_2 - m_1$. The main surface Π is depicted in Fig. 5. We can observe that the first quadrant is subdivided into 4 rectangles with lower left corner in $(0, 0)$. Therefore, the integral on Π can be computed as the sum of four integrals for each of the rectangles that have the lower-left corner at point $(0, 0)$ and the higher-right corner respectively at (m_2, n_2), (m_1, n_2), (m_2, n_1), and (m_1, n_1). Formula (16) can be used to each of these rectangles. In fact, by indicating with $[m_i, n_i]$ the aforementioned rectangles, for $i = 1, 2$, the integral I_{p1} of S can be written in polar coordinates as:

$$I_{p1} = I_{p1}^{[m_2,n_2]} - I_{p1}^{[m_1,n_2]} - I_{p1}^{[m_2,n_1]} + I_{p1}^{[m_1,n_1]}\,. \tag{19}$$

where the integrals $I_{p1}^{[m_i,n_i]}$ are computed as in (16) by using the position $l_1 = m_i$ and $l_2 = n_i$ for the integration extremes. Note that the equation (16) is valid only if $n_2 - n_1 < m_2 - m_2$, which requires that the 4 rectangles identified in Fig. 5 are such as:

$$n_1 < m_1, \quad n_1 < m_2, \quad n_2 < m_1, \text{ and } n_2 < m_2\,. \tag{20}$$

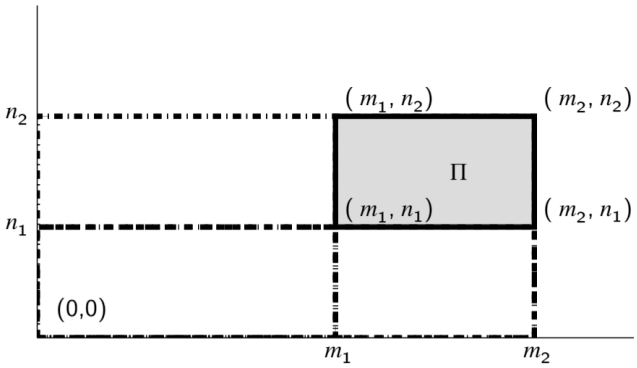

Figure 5: Surface Π in the first quadrant, $n_2 - n_1 < m_2 - m_1$.

If this condition does not hold and one of the rectangles is taller than wider, we have to switch the x and y coordinates as mentioned in the previous section. Summarizing, equation (19) holds true when the following 3 conditions are met:

1. $m_1 > 0\,, m_2 > 0\,, n_1 > 0\,, n_2 > 0\,;$
2. $n_2 - n_1 < m_2 - m_1\,;$ and
3. $n_1 < m_1, n_1 < m_2, n_2 < m_1,$ and $n_2 < m_2\,.$

Although equation (19) may seem unnecessarily complicated, on the contrary, it allows unifying the formula for all possible configurations. With a switch of coordinates when necessary and adopting proper sign management, we can bypass all the three conditions mentioned above, as clarified in the next section.

I_{p1} and sign management Equation (19) can be applied to all possible configurations by taking care of the signs of the integration extremes, as:

$$\begin{aligned} I_{p1} = {} & s_{m_1} s_{n_1} I_{p1}^{[m_2,n_2]} - s_{m_2} s_{n_1} I_{p1}^{[m_1,n_2]} \\ & - s_{m_1} s_{n_2} I_{p1}^{[m_2,n_1]} + s_{m_2} s_{n_2} I_{p1}^{[m_1,n_1]} \end{aligned} \tag{21}$$

where s_{m_i} and s_{n_i} for $i = 1, 2$ are defined as $\mathrm{sgn}(m_i)$ and $\mathrm{sgn}(n_i)$ respectively, and the sgn function defined as:

$$\mathrm{sgn}(x) = \begin{cases} 1 \text{ if } x \geq 0 \\ -1 \text{ if } x < 0 \end{cases}\,.$$

The central value of this formula is that it allows computing the integral I_{p1} for all possible plane configurations. In the following, we clarify the formula with the aid of 3 main scenarios, depicted in Fig. 6, being all others easily implied from them.

Case 0 In "Case 0", the plane is located in the first quadrant. Equation (21) reads as (19).

Case 1 In "Case 1", the plane is located between the first and the fourth quadrant. The partial rectangle that has the upright corner at point (m_2, n_1) must be summed, and the one that has the upright corner at point (m_1, n_1) must be subtracted. Equation (21) correctly applies by taking into account the negative sign of n_1.

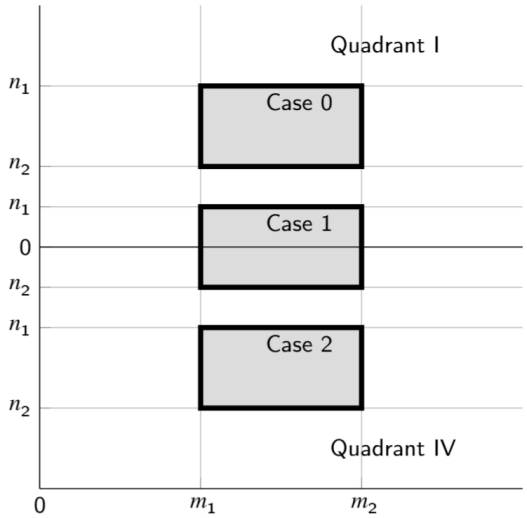

Figure 6: Three scenarios that are used to clarify the sign management used in eq. (21)

Case 2 In "Case 2", equation (21) would account for the negative sign of n_1 and n_2, and it reads as:

$$I_{p1} = -I_{p1}^{[m_2,n_2]} + I_{p1}^{[m_1,n_2]} + I_{p1}^{[m_2,n_1]} - I_{p1}^{[m_1,n_1]}. \tag{22}$$

This equation is the same as found for "Case 0", but with a negative sign. However, the original integral

$$I_{p1} = \int_{m_1}^{m_2} \int_{n_1}^{n_2} f(\hat{x},\hat{y})\, d\hat{y}\, d\hat{x} \tag{23}$$

has a negative sign as well, because $n_1 > n_2$, therefore its inner extremes are switched and the sign changed, as

$$I_{p1} = -\int_{m_1}^{m_2} \int_{n_2}^{n_1} f(\hat{x},\hat{y})\, d\hat{y}\, d\hat{x}. \tag{24}$$

Therefore, by taking into accout the negative sign in eq. (24), the eq. (22) will read as for "Case 0" as expected. All other cases are similarly treated. Algorithm 1 describes the steps for the computation of I_{p1} as pseudo-code.

3.1.3. Evaluation of I_{p2}

I_{p2} is hereby rewritten for convenience:

$$I_{p2} = \int_{m_1}^{m_2} \int_{n_1}^{n_2} (\hat{x} + K) f(\hat{x},\hat{y})\, d\hat{y}\, d\hat{x}. \tag{25}$$

The polar transformation in (12) allows writing I_{p2} in polar coordinates as

$$I_{p2} = \int_{D_\rho} \int_{D_\theta} (\rho\cos\theta + K) f(\rho)\, \rho\, d\rho\, d\theta. \tag{26}$$

We can first integrate with respect to θ and obtain

$$I_{p2} = \int_{D_\rho} \left(K\theta\Big|_{\theta_1(\rho)}^{\theta_2(\rho)} + \rho\sin\theta\Big|_{\theta_1(\rho)}^{\theta_2(\rho)} \right) f(\rho)\, \rho\, d\rho \tag{27}$$

Algorithm 1: Evaluation of I_{p1} as per eq. (21)

Data: Integration extremes m_1, m_2, n_1, n_2
Result: I_{p1}

```
s_{m_1} = sgn(m_1);
s_{m_2} = sgn(m_2);
s_{n_1} = sgn(n_1);
s_{n_2} = sgn(n_2);
for i ← 1 to 2 do
    for j ← 1 to 2 do
        if m_i < n_j then
            if |m_i| ≤ 0 then I_{p1}^{[m_i,n_j]} ⟵ 0;
            else
                Exchange x and y coordinates, n_j ⟵ m_i ;
                Compute the sub-integrals I_{p1}^{[m_i,n_j]} as per eq. (16);
            end
        else
            if |m_i| ≤ 0 then I_{p1}^{[m_i,n_j]} ⟵ 0;
            else Compute the sub-integrals I_{p1}^{[m_i,n_j]} as per eq. (16);
        end
    end
end
I_{p1} = s_{m_1} s_{n_1} I_{p1}^{[m_2,n_2]} − s_{m_2} s_{n_1} I_{p1}^{[m_1,n_2]} − s_{m_1} s_{n_2} I_{p1}^{[m_2,n_1]} + s_{m_2} s_{n_2} I_{p1}^{[m_1,n_1]};
return I_{p1};
```

where $D_\rho \neq D_\rho(\theta)$ does not depend on θ and is fixed. As similarly done for I_{p1} to get the equation (16), it is possible to show that

$$\begin{aligned} I_{p2} = &\underbrace{\int_0^{l_1} \left(K\theta\Big|_0^{\frac{\pi}{2}} + \rho\sin\theta\Big|_0^{\frac{\pi}{2}} \right) f(\rho)\rho\, d\rho}_{R_1} \\ &+ \underbrace{\int_{l_1}^{l_2} \left(K\theta\Big|_0^{\theta_2} + \rho\sin\theta\Big|_0^{\theta_2} \right) f(\rho)\, \rho\, d\rho}_{R_2} \\ &+ \underbrace{\int_{l_2}^{\sqrt{l_1^2+l_2^2}} \left(K\theta\Big|_{\theta_3}^{\theta_2} + \rho\sin\theta\Big|_{\theta_3}^{\theta_2} \right) f(\rho)\, \rho\, d\rho}_{R_3} \end{aligned} \tag{28}$$

with the same definitions for the integration extremes as given in Table 2. This result is valid if $l_1 < l_2$. For I_{p2}, the case for $l_1 > l_2$ requires further attention.

Basic rectangular case for $l_1 > l_2$ in I_{p2} As similarly done for I_{p1}, also for I_{p2} we can interchange the coordinates.

However, this means that

$$\widehat{x} = \rho \sin(\theta), \text{ and } \widehat{y} = \rho \cos(\theta).$$

Therefore, the integral is written as

$$\begin{aligned} I_{p2} &= \int_{D_\rho} \int_{D_\theta} (\rho \sin\theta + K) f(\rho)\ \rho\ d\rho\ d\theta \\ &= \int_{D_\rho} (K\theta\Big|_{\theta_1(\rho)}^{\theta_2(\rho)} - \rho\cos\theta\Big|_{\theta_1(\rho)}^{\theta_2(\rho)}) f(\rho)\ \rho\ d\rho \end{aligned} \tag{29}$$

In the following, the above integral I_{p2} for $l_1 > l_2$ will be called as "I_{p2}- type 2"; consequently, the integral I_{p2} for $l_1 < l_2$ will be called as "I_{p2}- type 1". For "I_{p2}- type 2", the equation (28) becomes:

$$\begin{aligned} I_{p2} = & \underbrace{\int_0^{l_1} (K\theta\Big|_0^{\frac{\pi}{2}} - \rho\cos\theta\Big|_0^{\frac{\pi}{2}}) f(\rho)\ \rho\ d\rho}_{R_1} \\ & + \underbrace{\int_{l_1}^{l_2} (K\theta\Big|_0^{\theta_2} - \rho\cos\theta\Big|_0^{\theta_2}) f(\rho)\ \rho\ d\rho}_{R_2} \\ & + \underbrace{\int_{l_2}^{\sqrt{l_1^2+l_2^2}} (K\theta\Big|_{\theta_3}^{\theta_2} - \rho\cos\theta\Big|_{\theta_3}^{\theta_2}) f(\rho)\ \rho\ d\rho}_{R_3} \end{aligned} \tag{30}$$

with the same definitions for the integration extremes as given in Table 2

I_{p2} and sign management By taking care of the signs of the coordinate swapping and the integration extremes, the integral I_{p2} is rewritten as:

$$I_{p2} = s_{n_1} I_{p2}^{[m_2,n_2]} - s_{n_1} I_{p2}^{[m_1,n_2]} - s_{n_2} I_{p2}^{[m_2,n_1]} + s_{n_2} I_{p2}^{[m_1,n_1]}. \tag{31}$$

Note that, due to the use of the cosines for $l_1 > l_2$, we do not need to account for the sign of m_1. Algorithm 2 describes the steps for the computation of I_{p2} as pseudo-code.

3.1.4. Evaluation of I_{p3}

I_{p3} is hereby rewritten for convenience:

$$I_{p3} = \int_{m_1}^{m_2} \int_{n_1}^{n_2} (\widehat{x} + K)(\widehat{y} + Q) f(\widehat{x}, y)\ d\widehat{y}\ d\widehat{x}. \tag{32}$$

The polar transformation in (12) allows writing I_{p3} in polar coordinates as

$$I_{p3} = \int_{D_\rho} \int_{D_\theta} (\rho\cos\theta + K)(\rho\sin\theta + Q) f(\rho)\ \rho\ d\rho\ d\theta. \tag{33}$$

We can first integrate with respect to θ and obtain

$$\begin{aligned} I_{p3} = \int_{D_\rho} \Bigg(& KQ\theta\Big|_{\theta_1(\rho)}^{\theta_2(\rho)} - K\rho\cos\theta\Big|_{\theta_1(\rho)}^{\theta_2(\rho)} \\ & + Q\rho\sin\theta\Big|_{\theta_1(\rho)}^{\theta_2(\rho)} - \frac{1}{2}\rho^2\cos\theta^2\Big|_{\theta_1(\rho)}^{\theta_2(\rho)} \Bigg) f(\rho)\ \rho\ d\rho \end{aligned} \tag{34}$$

where $D_\rho \neq D_\rho(\theta)$ does not depend on θ and is fixed. As similarly done for I_{p1} and I_{p2}, it is possible to show that

$$\begin{aligned} I_{p3} = & \underbrace{\int_0^{l_1} g\left(\rho, \theta\Big|_0^{\frac{\pi}{2}}\right) f(\rho)\ \rho\ d\rho}_{R_1} + \underbrace{\int_{l_1}^{l_2} g\left(\rho, \theta\Big|_0^{\theta_2}\right) f(\rho)\ \rho\ d\rho}_{R_2} \\ & + \underbrace{\int_{l_2}^{\sqrt{l_1^2+l_2^2}} g\left(\rho, \theta\Big|_{\theta_3}^{\theta_2}\right) f(\rho)\ \rho\ d\rho}_{R_3} \end{aligned} \tag{35}$$

where

$$g(\rho,\theta) = \left(KQ\theta - K\rho\cos\theta + Q\rho\sin\theta - \frac{1}{2}\rho^2\cos\theta^2 \right), \tag{36}$$

and with the same definitions for the integration extremes as given in Table 2. This result is valid if $l_1 < l_2$.

Basic rectangular case for $l_1 > l_2$ in I_{p3} As similarly done for I_{p2} we can swap the coordinates. However, for I_{p3}

Algorithm 2: Evaluation of I_{p2} as per eq. (31)

Data: Integration extremes m_1, m_2, n_1, n_2 and constant K as defined in Table 1
Result: I_{p2}

```
s_{m_1} = sgn(m_1);
s_{m_2} = sgn(m_2);
s_{n_1} = sgn(n_1);
s_{n_2} = sgn(n_2);
for i ← 1 to 2 do
    for j ← 1 to 2 do
        if m_i < n_j then
            Exchange x and y coordinates, n_j ⟵ m_i;
            if |m_i| ≤ 0 then I_{p2}^{[m_i,n_j]} ⟵ 0;
            else Compute the sub-integral I_{p2}^{[m_i,n_j]} as per eq. (30) ;
        else
            if |m_i| ≤ 0 then I_{p2}^{[m_i,n_j]} ⟵ 0;
            else Compute the sub-integrals I_{p2}^{[m_i,n_j]} as per eq. (28);
        end
    end
end
I_{p2} = s_{n_1} I_{p2}^{[m_2,n_2]} − s_{n_1} I_{p2}^{[m_1,n_2]} − s_{n_2} I_{p2}^{[m_2,n_1]} + s_{n_2} I_{p2}^{[m_1,n_1]};
return I_{p2};
```

Table 3
Sign and type management for integral I_{p3}, for $i = 1, 2$.

Sub-integral	type-1	type-2
$I_{p3}^{[m_i,n_i]}$	$K = s_{m_i}K\,, Q = s_{n_i}Q$	$K = s_{n_i}Q\,, Q = s_{m_i}K$

the formula reads the same, except that the K and Q are exchanged, namely $K = Q$ and $Q = K$. In the following, the above integral I_{p3} for $l_1 > l_2$ will be called as "I_{p3}- type 2"; consequently, the integral I_{p3} for $l_1 < l_2$ will be called as "I_{p3}- type 1".

I_{p3} and sign management For I_{p3}, the sign management involves only the $g(\rho, \theta)$ function (36). In fact, the formula reads as

$$I_{p3} = I_{p3}^{[m_2,n_2]} - I_{p3}^{[m_1,n_2]} - I_{p3}^{[m_2,n_1]} + I_{p3}^{[m_1,n_1]}, \tag{37}$$

where the 4 sub-integrals account for the variable change and the sign management as summarized in Table 3. Algorithm 3 describes the steps for the computation of I_{p3} as pseudo-code.

3.2. Summary of the quadruple integral computation for parallel surfaces

Summarizing, in the parallel case, the quadruple integral can be expressed as a sum of 9 double integrals as in eq. (10). By following the notation given, we can write the integral as

$$\begin{aligned} I_{H,p} = {} & I_{p3,R_{11}} + Q_2 I_{p2,R_{12}} - I_{p3,R_{13}} + K_2 I_{p2,R_{21}} \\ & + K_2 Q_2 I_{p1,R_{22}} - K_2 I_{p2,R_{23}} - I_{p3,R_{31}} \\ & - Q_2 I_{p2,R_{32}} + I_{p3,R_{33}}\,. \end{aligned} \tag{38}$$

Each integral can be expressed as a sum of 12 single integrals, by using formula (21) for the generic I_{p1}, formula (31) for the generic I_{p2}, and formula (37) for the generic I_{p3}. To conclude, the quadruple integral has been decomposed into the sum of $12 \times 9 = 108$ single integrals. Algorithm 4 summarizes all the steps as pseudo-code.

Algorithm 3: Evaluation of I_{p3} as per eq. (31)

Data: Integration extremes m_1, m_2, n_1, n_2 and constants K, Q as defined in Table 1
Result: I_{p3}

```
s_{m_1} = sgn(m_1);
s_{m_2} = sgn(m_2);
s_{n_1} = sgn(n_1);
s_{n_2} = sgn(n_2);
for i ← 1 to 2 do
    for j ← 1 to 2 do
        if m_i < n_j then
            Exchange x and y coordinates, n_j ⟵ m_i;
            if |m_i| ≤ 0 then I_{p3}^{[m_i,n_j]} ⟵ 0;
            else
                Exchange K and Q such as K ⟵ s_{n_i} Q and Q ⟵ s_{m_i} K (see Table 3, type-2);
                Compute the sub-integral I_{p3}^{[m_i,n_j]} as per eq. (35);
            end
        else
            if |m_i| ≤ 0 then I_{p3}^{[m_i,n_j]} ⟵ 0;
            else
                K ⟵ s_{m_i} K and Q ⟵ s_{n_i} Q (see Table 3, type-1);
                Compute the sub-integrals I_{p3}^{[m_i,n_j]} as per eq. (28);
            end
        end
    end
end
I_{p3} = I_{p3}^{[m_2,n_2]} - I_{p3}^{[m_1,n_2]} - I_{p3}^{[m_2,n_1]} + I_{p3}^{[m_1,n_1]};
return I_{p3};
```

4. Decomposition of the quadruple integral I_H - orthogonal surfaces

Figure 7 shows 2 orthogonal rectangles in the 3D space:

$$\Pi = \left\{(x, y, z) \in \mathbb{R}^3 |\ x_1 \le x \le x_2,\ y_1 \le y \le y_2,\ z = z_1\right\},$$

$$\Pi' = \left\{(x', y', z') \in \mathbb{R}^3 |\ x_3 \le x' \le x_4,\ y' = y_3,\ z_3 \le z' \le z_4\right\}.$$

In the orthogonal case, the 3rd component z is fixed in the Π domain as $z = z_1$, and the 2nd component y is fixed in the Π' domain as $y = y_3$. The 4D integral (2) to be solved is written as

$$I_{H,o} = \int_{\Pi}\int_{\Pi'} \frac{1}{R} \mathrm{e}^{-j\beta R}\, dz'\, dx'\, dy\, dx \tag{39}$$

where the subscript "o" is for "orthogonal", and R is equal to

$$R = \sqrt{(x - x')^2 + (y - y_3)^2 + (z_1 - z')^2}\,. \tag{40}$$

In the parallel case, the 4D integral was written as a sum of 9 double integrals. In the orthogonal case, the 4D integral can be written as a sum of 3 triple integrals, and the steps that follow closely resemble the ones for the parallel case. Following the same reasoning as for the parallel case, we can perform a change of variable for the x component, such as $\hat{x} = x - x'$, and the integral in the x-variable is as in (7). The integral in the $\hat{x}$ and x variables is written as in (9) for the case $|x_3 - x_4| > |x_2 - x_1|$. To avoid different geometries in $(\hat{x}, x)$-domain (see Fig. 2-3), the case $|x_3 - x_4| < |x_2 - x_1|$ is solved by swapping $x \leftrightarrow x'$ and so by reducing to the previous one. To simplify and unify the notation, we

Algorithm 4: Evaluation of I_p as per eq. (38)

Data: $X_1, X_2, X_3, X_4, Y_1, Y_2, Y_3, Y_4, K_1, K_2, K_3, Q_1, Q_2, Q_3$ as per Table 1
Result: I_p

$I_{p3,R_{11}} \longleftarrow$ as per Alg. 3, with input data $X_1, X_2, Y_1, Y_2, K_1, Q_1$;
$I_{p2,R_{12}} \longleftarrow$ as per Alg. 2, with input data X_1, X_2, Y_2, Y_3, K_1;
$I_{p3,R_{13}} \longleftarrow$ as per Alg. 3, with input data $X_1, X_2, Y_3, Y_4, K_1, -Q_3$;
$I_{p2,R_{21}} \longleftarrow$ as per Alg. 2, with input data Y_1, Y_2, X_2, X_3, Q_1;
$I_{p1,R_{22}} \longleftarrow$ as per Alg. 1, with input data X_2, X_3, Y_2, Y_3;
$I_{p2,R_{23}} \longleftarrow$ as per Alg. 2, with input data $Y_3, Y_4, X_2, X_3, -Q_3$;
$I_{p3,R_{31}} \longleftarrow$ as per Alg. 3, with input data $X_3, X_4, Y_1, Y_2, -K_3, Q_1$;
$I_{p2,R_{32}} \longleftarrow$ as per Alg. 2, with input data $X_3, X_4, Y_2, Y_3, -K_3$;
$I_{p3,R_{33}} \longleftarrow$ as per Alg. 3, with input data $X_3, X_4, Y_3, Y_4, -K_3, -Q_3$;
Evaluate $I_p = I_{p3,R_{11}} + Q_2 I_{p2,R_{12}} - I_{p3,R_{13}} + K_2 I_{p2,R_{21}} + K_2 Q_2 I_{p1,R_{22}} - K_2 I_{p2,R_{23}} - I_{p3,R_{31}} - Q_2 I_{p2,R_{32}} + I_{p3,R_{33}}$;
return I_p;

introduce the shifted y, z-variables as follows:

$$\hat{y} = y - y_3,\ \hat{z} = z_1 - z' .$$

The corresponding 2D integrals read as

$$\int_{y_1}^{y_2}\int_{z_3}^{z_4} f(y - y_3, z_1 - z')\, dz'\, dy = \int_{y_1-y_3}^{y_2-y_3}\int_{z_1-z_4}^{z_1-z_3} f(\hat{y},\hat{z})\, d\hat{y}\, d\hat{z}. \tag{41}$$

Finally, the integral in the orthogonal case can be written as

$$\begin{aligned}\int_{\Pi}\int_{\Pi'} f(x - x', y - y_3, z_1 - z')\, dz'\, dx'\, dy\, dx = \\ \underbrace{\int_{X_1}^{X_2}\int_{Y_1}^{Y_2}\int_{Z_1}^{Z_2} f(\hat{x},\hat{y},\hat{z})(\hat{x} + K_1)\, d\hat{z}\, d\hat{y}\, d\hat{x}}_{R_1} \\ + K_2 \underbrace{\int_{X_2}^{X_3}\int_{Y_1}^{Y_2}\int_{Z_1}^{Z_2} f(\hat{x},\hat{y},\hat{z})\, d\hat{z}\, d\hat{y}\, d\hat{x}}_{R_2} \\ + \underbrace{\int_{X_3}^{X_4}\int_{Y_1}^{Y_2}\int_{Z_1}^{Z_2} f(\hat{x},\hat{y},\hat{z})(K_3 - \hat{x})\, d\hat{z}\, d\hat{y}\, d\hat{x}}_{R_3}\end{aligned} \tag{42}$$

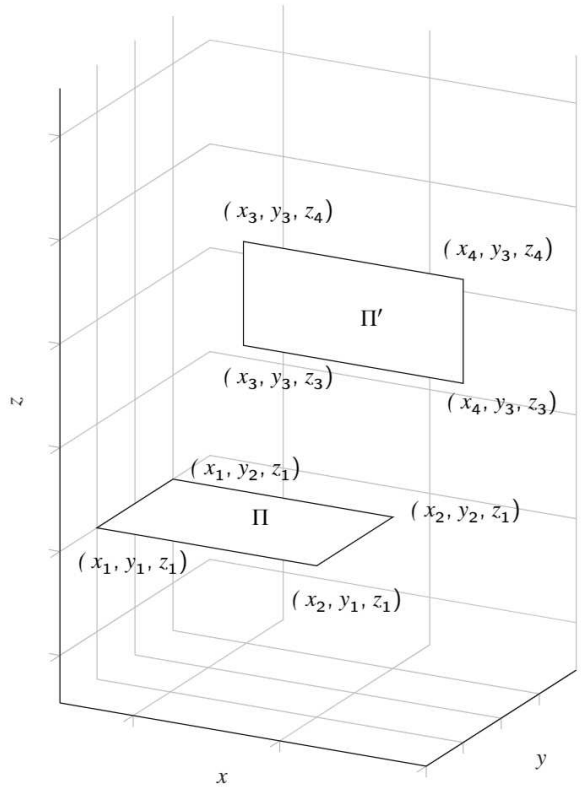

Figure 7: Two generic orthogonal surfaces.

Table 4
Constants used in eq. (42) for the orthogonal case

$X_1 = x_1 - x_4$	$Y_1 = y_1 - y_3$	$Z_1 = z_1 - z_4$	$K_1 = x_4 - x_1$
$X_2 = x_2 - x_4$	$Y_2 = y_2 - y_3$	$Z_2 = z_1 - z_3$	$K_2 = x_2 - x_1$
$X_3 = x_1 - x_3$			$K_3 = x_2 - x_3$
$X_4 = x_2 - x_3$			

where the integration extremes and the constants are defined in Table 4 as similarly done for the parallel case. The evaluation of integral (42) requires the solution of the following two main types of triple integrals:

$$I_{o1,R_2} = \int_{m_1}^{m_2}\int_{n_1}^{n_2}\int_{w_1}^{w_2} f(\hat{x},\hat{y},\hat{z})\, d\hat{z}\, d\hat{y}\, d\hat{x}, \tag{43a}$$

$$I_{o2,R_i} = \int_{m_1}^{m_2}\int_{n_1}^{n_2}\int_{w_1}^{w_2} (\hat{x} + K) f(\hat{x},\hat{y},\hat{z})\, d\hat{z}\, d\hat{y}\, d\hat{x},\ i = 1, 3 \tag{43b}$$

where the generic integration extremes m, n, and w are the X, Y and Z extremes, respectively, of the corresponding integral type in (42). The subscript R_i will be omitted unless necessary.

4.1. Cylindrical coordinates and radial behavior - orthogonal surfaces

As similarly done for the parallel case, in the following section we provide the representation in cylindrical coordinates of the two integrals in (43a).

4.1.1. Evaluation of I_{o1}

In this section, the integral I_{o1} in (43a) is rewritten in cylindrical coordinates. By taking the x and y coordinate as in (12), we can write

$$I_{o1} = \int_{m_1}^{m_2}\int_{n_1}^{n_2}\int_{w_1}^{w_2} f(\hat{x},\hat{y},\hat{z})\, d\hat{z}\, d\hat{y}\, d\hat{x} = \int_{w_1}^{w_2}\int_{D_\rho}\int_{D_\theta} f(\rho,\hat{z})\, \rho\, d\rho\, d\theta\, d\hat{z} \tag{44}$$

where the transformed function $f(\rho,\hat{z})$ is

$$f(\rho,\hat{z}) = \frac{\mathrm{e}^{-j\beta\sqrt{\rho^2+\hat{z}^2}}}{\sqrt{\rho^2+\hat{z}^2}}. \tag{45}$$

Following similar steps as for I_{p1}, it is possible to prove that the integral in (44) can be expressed as a sum of 3 integrals, as:

$$I_{o1} = \underbrace{\int_{w_1}^{w_2}\int_{0}^{l_1} f(\rho,\hat{z})\, \rho\, d\hat{z}\cdot\theta\Big|_0^{\frac{\pi}{2}}}_{I_{o11}} + \int_{w_1}^{w_2}\int_{l_1}^{l_2} f(\rho,\hat{z})\, \rho\, d\hat{z}\cdot\theta\Big|_0^{\theta_2} + \int_{w_1}^{w_2}\int_{l_2}^{\sqrt{l_1^2+l_2^2}} f(\rho,\hat{z})\, \rho\, d\hat{z}\cdot\theta\Big|_{\theta_3}^{\theta_2} \tag{46}$$

with the same definition of the integration extremes provided in Table 2. In this case, we provide the 1D expression only for the first integral in (46), called I_{o11}, and the other two integrals are left as double integral. In fact, the corresponding single integrals would involve several terms with logarithms, inverse tangent and tangent that may cause numerical and convergence problems. Note that the integral I_{o11} refers to the generic rectangle $[0, n_i]$.

Decomposition of I_{o11} The integral I_{o11} can be conveniently rewritten as:

$$I_{o11} = \frac{\pi}{2}\int_{w_1}^{w_2}\int_{0}^{l_1} f(\rho,\hat{z})\, \rho\, d\rho\, d\hat{z}. \tag{47}$$

By using the following cylindrical coordinate transformation

$$\rho = t\cos(\phi),\ \text{and}\ \hat{z} = t\sin(\phi)$$

with $t = \sqrt{\rho^2+\hat{z}^2}$, $\phi = \arctan\left(\frac{\hat{z}}{\rho}\right)$, we can write I_{o11} as it was done for I_{p1} in (15) as

$$I_{o11} = \frac{\pi}{2}\int_{D_t}\int_{D_\phi} \cos(\phi) e^{-j\beta t} t\, dt\, d\phi = \frac{\pi}{2}\int_{D_t} t\sin(\phi)\Big|_{\phi_1(t)}^{\phi_2(t)} \mathrm{e}^{-j\beta t} dt. \tag{48}$$

The integral (48) closely resembles the integral I_{p1} in (15), and it can be computed as the sum of two rectangles as the one depicted in Fig. (4). For first rectangle, l_1 is equal to w_1, and for the second rectangle, l_2 is equal to w_2, such as

$$I_{o11} = -I_{o11^{(w_1)}} + I_{o11^{(w_2)}}. \tag{49}$$

In the same way as done for I_{p1}, it is possible to prove that

$$I_{o11^{(w_i)}} = \frac{\pi}{2}\left[\int_0^{w_i} t\mathrm{e}^{-j\beta t}\, dt\cdot\sin(\phi)\Big|_0^{\frac{\pi}{2}} + \int_{w_i}^{l_1} t\mathrm{e}^{-j\beta t}\, dt\cdot\sin(\phi)\Big|_0^{\phi_2} + \int_{l_1}^{\sqrt{w_i^2+l_1^2}} t\mathrm{e}^{-j\beta t}\, dt\cdot\sin(\phi)\Big|_{\phi_3}^{\phi_2}\right] \tag{50}$$

where the integration extremes are defined as per Table 2 by substituting ρ with t and θ with ϕ. The same reasoning for $l_1 > l_2$ in I_{p1} can be applied in this case as well, and the general expression for the integral I_{o11} is

$$I_{o11} = -s_{w_1} I_{o11^{(w_1)}} + s_{w_2} I_{o11^{(w_2)}} \tag{51}$$

with s_{w_i} defined as the $\mathrm{sgn}(w_i)$, for $i = 1, 2$. Algorithm 5 describes the steps for the computation of I_{o11} as pseudo-code.

Algorithm 5: Evaluation of I_{o11} as per eq. (51)

Data: Integration extremes l_1, w_1, w_2
Result: I_{o11}

```
s_{w_1} = sgn(w_1);
s_{w_2} = sgn(w_2);
for i ← 1 to 2 do
    if (w_i < l_1 and w_i > 0) or (w_i ≥ l_1 and l_1 > 0) then
        Evaluate I_{o11^(w_1)} as per eq. (50) ;
    else I_{o11^(w_1)} ⟵ 0;
end
I_{o11} = −s_{w_1} I_{o11^(w_1)} + s_{w_2} I_{o11^(w_2)};
return I_{o11};
```

Sign management for I_{o1} Following the same reasoning as for I_{p1}, the final expression of I_{o1} is

$$I_{o1} = s_{m_1}s_{n_1} I_{o1}^{[m_2,n_2]} - s_{m_2}s_{n_1} I_{o1}^{[m_1,n_2]} - s_{m_1}s_{n_2} I_{o1}^{[m_2,n_1]} + s_{m_2}s_{n_2} I_{o1}^{[m_1,n_1]}, \tag{52}$$

where the generic $I_{o1}^{[m_i,n_i]}$ is computed as per eq. (46). Algorithm 6 describes the steps for the computation of I_{o1} as pseudo-code.

4.2. Evaluation of I_{o2}

The integral I_{o2} can be written in cylindrical coordinates as

$$I_{o2} = \int_{m_1}^{m_2}\int_{n_1}^{n_2}\int_{w_1}^{w_2} f(\hat{x},\hat{y},\hat{z})\, d\hat{z}\, d\hat{y}\, d\hat{x}$$

$$= \int_{w_1}^{w_2} \int_{D_\rho} \int_{D_\theta} (\rho \cos\theta + k) f(\rho, \hat{z})\ \rho\ d\rho\ d\theta\ d\hat{z} \quad (53)$$

with the same definition of the original and transformed functions as for I_{o1}. We can integrate with respect to θ and obtain

$$I_{o2} = \int_{w_1}^{w_2} \int_{D_\rho} f(\rho, z) \left(\rho \sin\theta \Big|_{\theta_1(\rho)}^{\theta_2(\rho)} + k\theta \Big|_{\theta_1(\rho)}^{\theta_2(\rho)} \right) \rho\ d\rho\ d\hat{z}\,. \quad (54)$$

Following similar steps as for I_{p1}, it is possible to prove that the integral in (44) can be expressed as a sum of 3 integrals, as:

$$I_{o2} = \underbrace{\int_{w_1}^{w_2} \int_{0}^{l_1} f(\rho, \hat{z}) \left(\rho \sin\theta \Big|_{0}^{\frac{\pi}{2}} + k\theta \Big|_{0}^{\frac{\pi}{2}} \right) \rho\ d\rho\ d\hat{z}}_{I_{o21}}$$
$$+ \int_{w_1}^{w_2} \int_{l_1}^{l_2} f(\rho, \hat{z}) \left(\rho \sin\theta \Big|_{0}^{\theta_2} + k\theta \Big|_{0}^{\theta_2} \right) \rho\ d\rho\ d\hat{z}$$
$$+ \int_{w_1}^{w_2} \int_{l_2}^{\sqrt{l_1^2+l_2^2}} f(\rho, \hat{z}) \left(\rho \sin\theta \Big|_{\theta_3}^{\theta_2} + k\theta \Big|_{\theta_3}^{\theta_2} \right) \rho\ d\rho\ d\hat{z} \quad (55)$$

with the same definition of the integration extremes provided in Table 2. It is possible to further simplify the integral I_{o21} as follows. Similarly as for the I_{o1}, we provide the 1D expression only for the first integral in (55), called I_{o21}, and the other two integrals are left as double integral. In fact, the corresponding single integrals would involve several terms with logarithms, inverse tangent and tangent that may cause numerical and convergence problems.

Algorithm 6: Evaluation of I_{o1} as per eq. (52)

Data: Integration extremes $m_1, m_2, n_1, n_2, w_1, w_2$
Result: I_{o1}

$s_{m_1} = \text{sgn}(m_1)$;
$s_{m_2} = \text{sgn}(m_2)$;
$s_{n_1} = \text{sgn}(n_1)$;
$s_{n_2} = \text{sgn}(n_2)$;
for $i \leftarrow 1$ **to** 2 **do**
  for $j \leftarrow 1$ **to** 2 **do**
    if $m_i < n_j$ **then**
      if $|m_i| \leq 0$ **then** $I_{o1}^{[m_i,n_j]} \longleftarrow 0$;
      else
        Exchange x and y coordinates, $n_j \longleftarrow m_i$;
        The term I_{o11} in eq. (50) is computed as by using Alg. 5 with input parameters m_i, w_1, w_2;
        Compute the 2 double integrals in eq. (46);
        Compute the sub-integral I_{o1} as the sum of I_{o11} and the 2 double integrals ;
      end
    else
      if $|m_i| \leq 0$ **then** $I_{o1}^{[m_i,n_j]} \longleftarrow 0$;
      else
        The term I_{o11} in eq. (50) is computed as by using Alg. 5 with input parameters m_i, w_1, w_2;
        Compute the 2 double integrals in eq. (46);
        Compute the sub-integral I_{o1} as the sum of I_{o11} and the 2 double integrals ;
      end
    end
  end
end
Compute $I_{o1} = s_{m_1} s_{n_1} I_{o1}^{[m_2,n_2]} - s_{m_2} s_{n_1} I_{o1}^{[m_1,n_2]} - s_{m_1} s_{n_2} I_{o1}^{[m_2,n_1]} + s_{m_2} s_{n_2} I_{o1}^{[m_1,n_1]}$;
return I_{o1};

Decomposition of I_{o21} The integral I_{o21} can be conveniently rewritten as:

$$I_{o21} = \int_{w_1}^{w_2} \int_{0}^{l_1} \left(k\frac{\pi}{2} + \rho \right) f(\rho, \hat{z})\ \rho\ d\rho\ d\hat{z}\,. \quad (56)$$

By using the polar transformation, we can write the integral as:

$$I_{o21} = \int_{0}^{l_1} \int_{D_\phi} \left(k\frac{\pi}{2} + t\cos(\phi) \right) \cos(\phi)\ \mathrm{e}^{-j\beta t} t\ dt\ d\phi$$
$$= \int_{0}^{l_1} \left(\phi\frac{t}{2} + k\frac{\pi}{2}\sin(\phi) + \frac{t}{4}\sin(2\phi) \right) \Big|_{\phi_1(t)}^{\phi_2(t)} t\,\mathrm{e}^{-j\beta t} dt \quad (57)$$

Similarly to the integral for I_{o11}, the integral (57) closely resembles the integral I_{p1} in (15), and it can be computed as the sum of two rectangles as the one depicted in Fig. (4). For first rectangle, l_1 is equal to w_1, and for the second rectangle, l_2 is equal to w_2, such as:

$$I_{o21} = -I_{o21^{(w_1)}} + I_{o21^{(w_2)}}\,. \quad (58)$$

As done for I_{p1}, it is possible to prove that

$$I_{o21^{(w_i)}} = \int_{0}^{w_i} h(t,\phi) \Big|_{0}^{\frac{\pi}{2}}\ dt + \int_{w_i}^{l_1} h(t,\phi) \Big|_{0}^{\phi_2}\ dt$$
$$+ \int_{l_1}^{\sqrt{w_i^2+l_1^2}} h(t,\phi) \Big|_{\phi_3}^{\phi_2}\ dt \quad (59)$$

where $h(t,\phi) = \left(\phi\frac{t}{2} + k\frac{\pi}{2}\sin\phi + \frac{t}{4}\sin 2\phi \right) te^{-j\beta t}$, and the integration extremes are defined as per Table 2 by substituting ρ with t and θ with ϕ. The same reasoning for $l_1 > l_2$ in I_{p1} can be applied in this case as well, and the general expression for the integral I_{o11} is

$$I_{o21} = -s_{w_1} I_{o21^{(w_1)}} + s_{w_2} I_{o21^{(w_2)}} \quad (60)$$

with s_{w_i} defined as the $\mathrm{sgn}(w_i)$, for $i = 1, 2$.

Algorithm 7 describes the steps for the computation of I_{o21} as pseudo-code.

Algorithm 7: Evaluation of I_{o21} as per eq. (60)

Data: Integration extremes l_1, w_1, w_2
Result: I_{o21}
$s_{w_1} = \mathrm{sgn}(w_1)$;
$s_{w_2} = \mathrm{sgn}(w_2)$;
for $i \leftarrow 1$ **to** 2 **do**
  if *($w_i < l_1$* **and** *$w_i > 0$)* **or** *($w_i \geq l_1$* **and** *$l_1 > 0$)* **then**
    Evaluate $I_{o21^{(w_1)}}$ as per eq. (59) ;
  else $I_{o21^{(w_1)}} \longleftarrow 0$;
end
$I_{o21} = -s_{w_1} I_{o21^{(w_1)}} + s_{w_2} I_{o21^{(w_2)}}$;
return I_{o11};

Basic rectangular case for $l_1 > l_2$ in I_{o2} Similarly as for the integral I_{p2}, if $l_1 > l_2$, we can swap the coordinates. The integral I_{o2} can be written as

$$I_{o2} = \int_{w_1}^{w_2} \int_{\rho} \int_{\theta} (\rho \sin\theta + k) f(\rho, \hat{z})\ \rho\ d\rho\ d\theta\ d\hat{z} = \int_{w_1}^{w_2} \int_{D_\rho} f(\rho, z) \left(k\theta \Big|_{\theta_1(\rho)}^{\theta_2(\rho)} - \rho \cos\theta \Big|_{\theta_1(\rho)}^{\theta_2(\rho)} \right)\ \rho\ d\rho\ d\hat{z}\,. \tag{61}$$

The integral in (55) can be rewritten accordingly. For I_{o21}, the function $h(t, \phi)$ in (59) reads as

$$h(t, \phi) = \left(\phi \frac{t}{2} - k \frac{\pi}{2} \cos\phi - \frac{t}{4} \cos 2\phi \right) t e^{-j\beta t}\,.$$

Sign management for I_{o2} Following the same reasoning as for I_{p2}, the final expression for the integral I_{o2} is

$$I_{o2} = s_{n_1} I_{o2}^{[m_2,n_2]} - s_{n_1} I_{o2}^{[m_1,n_2]} - s_{n_2} I_{o2}^{[m_2,n_1]} + s_{n_2} I_{o2}^{[m_1,n_1]}, \tag{62}$$

where the generic $I_{o2}^{[m_i,n_i]}$ is computed as

$$I_{o21}^{[m_i,n_i]} = s_{w_1} I_{o21^{(w_1)}} - s_{w_2} I_{o21^{(w_2)}}\,. \tag{63}$$

In the following, the above integral I_{02} for $l_1 > l_2$ will be called as "I_{o2}- type 2"; consequently, the integral I_{o2} for $l_1 < l_2$ will be called as "I_{o2}- type 1". Algorithm 8 describes the steps for the computation of I_{o2} as pseudo-code.

Algorithm 8: Evaluation of I_{o2} as per eq. (62)

Data: Integration extremes $m_1, m_2, n_1, n_2, w_1, w_2, k$
Result: I_{o2}
$s_{m_1} = \mathrm{sgn}(m_1)$;
$s_{m_2} = \mathrm{sgn}(m_2)$;
$s_{n_1} = \mathrm{sgn}(n_1)$;
$s_{n_2} = \mathrm{sgn}(n_2)$;
for $i \leftarrow 1$ **to** 2 **do**
  for $j \leftarrow 1$ **to** 2 **do**
    if $m_i < n_j$ **then**
      if $|m_i| \leq 0$ **then** $I_{o2}^{[m_i,n_j]} \longleftarrow 0$;
      else
        Exchange x and y coordinates, $n_j \longleftarrow m_i$;
        The term I_{o21} in eq. (59) is computed as by using Alg. 7 with input parameters m_i, w_1, w_2;
        Compute the 2 double integrals in eq. (55);
        Compute the sub-integral I_{o2} as the sum of I_{o21} and the 2 double integrals ;
      end
    else
      if $|m_i| \leq 0$ **then** $I_{o2}^{[m_i,n_j]} \longleftarrow 0$;
      else
        The term I_{o21} in eq. (59) is computed as by using Alg. 7 with input parameters m_i, w_1, w_2;
        Compute the 2 double integrals in eq. (55);
        Compute the sub-integral I_{o2} as the sum of I_{o21} and the 2 double integrals ;
      end
    end
  end
end
Compute $I_{o2} = s_{n_1} I_{o2}^{[m_2,n_2]} - s_{n_1} I_{o2}^{[m_1,n_2]} - s_{n_2} I_{o2}^{[m_2,n_1]} + s_{n_2} I_{o2}^{[m_1,n_1]}$;
return I_{o1};

4.3. Summary for orthogonal surfaces

Summarizing, in the orthogonal case the quadruple integral can be expressed as a sum of 3 integrals as

$$I_o = I_{o2,R_1} + K_2 I_{o1,R_2} - I_{o2,R_3}\,. \tag{64}$$

Each integral I_{o1} and I_{o2} is expressed each as a sum of 24 single integrals and 8 double integrals. For I_{o1}, we use the formula in (52), and for the generic I_{o2} we use formula (62). It follows that the quadruple integral in (39) has been decomposed into the sum of 72 single integrals and 24 double integrals. Algorithm 9 summarizes all the steps as pseudo-code.

5. Numerical examples

The proposed formulas are tested for rectangles Π and Π' that are parallel and orthogonal to each other. For the parallel case, we compare the original quadruple integral (4)

Algorithm 9: Evaluation of I_p as per eq. (38)

Data: $X_1, X_2, Y_1, Y_2, Z_1, Z_2, K_1, K_2, K_3$ as per Table 4

Result: I_o

$I_{o2,R_1} \longleftarrow$ as per Alg. 8, with input data $X_1, X_2, Y_1, Y_2, Z_1, Z_2, K_1$;

$I_{o1,R_2} \longleftarrow$ as per Alg. 6, with input data $X_2, X_3, Y_1, Y_2, Z_1, Z_2$;

$I_{o2,R_3} \longleftarrow$ as per Alg. 8 , with input data $X_3, X_4, Y_1, Y_2, Z_1, Z_2, -K_3$;

Evaluate $I_o = I_{o2,R_1} + K_2 I_{o1,R_2} - I_{o2,R_3}$;

return I_o;

with the proposed decoupled integral in equation (38). For the orthogonal case, we compare the original quadruple integral (39) with the proposed decoupled integral in equation (64). The integrals computed with the proposed decoupling formulation (equation (38) in the parallel case, and equation (64) in the orthogonal case) are named I_{dec}. The original quadruple integrals (equation (4) in the parallel case, and equation (39) in the orthogonal case) are used as a reference value and named I_{ref}. The software used is Matlab®, version R2020a, running on a machine with OS Windows® 10, with 4 cores and 8 logical processors. The single and double integrals used in the proposed formulation are computed with the Matlab® functions `integral` and `integral2`, respectively. The quadruple integrals are computed with the Matlab® function `integralN` [33], which uses `integral2` and `integral3` functions iteratively to perform integrals of order 4, 5, and 6. We provide the speedup of I_{ref} compared with I_{dec}. Note that the absolute running time is not relevant because the code is not optimized, and the focus is to support the validation of the proposed decoupling approach. The proposed derivation does not involve any approximation. Therefore, strictly mathematically speaking, the quadruple integral is equal to the decoupled integral. However, from a numerical point of view, small differences will arise due to the numerical accuracy reached for each decoupled integral. When computing numerical integrals, a critical role is played by the relative and absolute tolerances used. They determine both the accuracy and the computational speed because requesting a high accuracy will slow down the computation, and a fast computation will penalize the accuracy of the solution. The examples consider realistic patch sizes as they occur in typical EM modeling geometries, and the related integrals have a small absolute value; therefore, the absolute error is the critical value for the accuracy. We use an absolute error tolerance[1] of 10^{-12} and leave the default value of 10^{-6} for relative error tolerance. We adopted the same absolute error for all the decoupled integrals. In the simulation results, we take into account the numerical differences between the I_{ref} and I_{dec} by defining the normwise

[1] https://se.mathworks.com/help/matlab/ref/integral.html

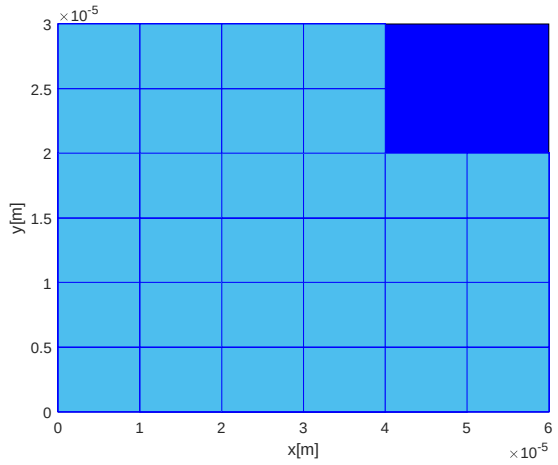

Figure 8: Mesh used to test several combinations in the parallel case, for $d_z = 0$.

relative error between I_{ref} and I_{dec}:

$$\epsilon = \frac{|I_{ref} - I_{dec}|}{|I_{ref}|}, \quad \text{for } |I_{ref}| \neq 0. \tag{65}$$

Noticeably, the computation of the quadruple integral was issuing warnings for close-to-singular kernels (near patches), whereas the decoupled integrals did not.

5.1. Parallel rectangles

In this section, we show the acceleration provided with the proposed formula in (38) against the standard 4D formula (4), for the parallel case, and provide the normwise errors. We consider a subset of possible scenarios, with rectangle Π that is fixed in the xy-plane. In the examples, Π is in dark blue. We build a rectangular mesh made of elementary patches. The interaction integrals are evaluated between Π and the possible Π' resulting from the mesh, given by the patches plus their combinations that result in a rectangle. Given a generic grid with N_x patches on the x-direction, and N_y patches on the y-direction, the total number of combinations P that result in a rectangle or in a square can be computed as:

$$P = \sum_{k=0}^{N_y-1} \sum_{c=1}^{N_x} (N_x - c + 1) \cdot (N_y - k). \tag{66}$$

The distance between Π and the mesh is either $d_z = 0$ or $d_z \neq 0$, as depicted in Figures 8 and 9, for a particular case with 32 and 36 patches, respectively.

5.1.1. Parallel mesh. Conductor interior problem

In this section, we consider the conductor interior problem, with $\epsilon_r = 1$ and $\sigma = 5.8 \times 10^7$ [S/m] (copper). The standard integral and the decoupled integral are solved for 10 frequency points, for the meshes depicted in Fig. 8 and 9. The interaction integrals are computed between the main rectangle and the patches plus all possible combinations of them

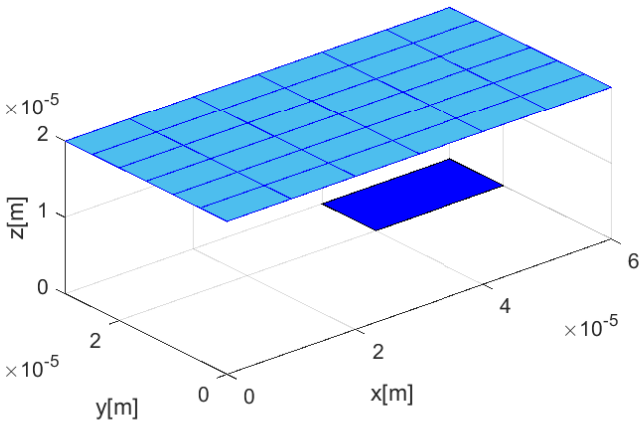

Figure 9: Mesh used to test several combinations in the parallel case, for $d_z = 20\,\mu\text{m}$.

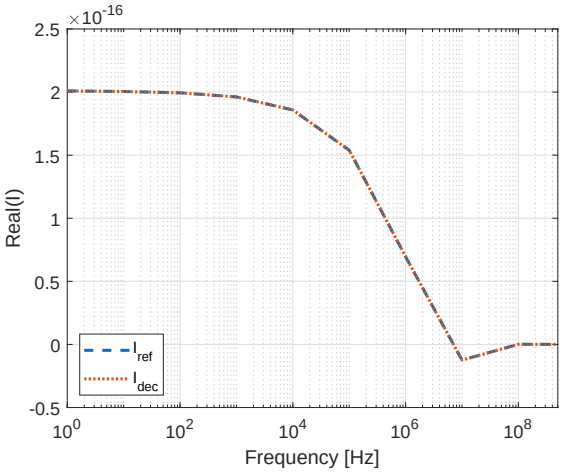

Figure 11: Real part of the integrals for the parallel mesh with 681 combinations, conductor case.

Table 5
Computational time for different parallel meshes (conductor case), for 10 logarithmic-spaced frequency points in the interval .

Numb. of configurations	681	2115	9031
Computational time I_{ref}	30 min	2 h	6 h
Computational time I_{dec}	1.5 min	6 min	30 min
Acceleration	× 20	× 15	× 12

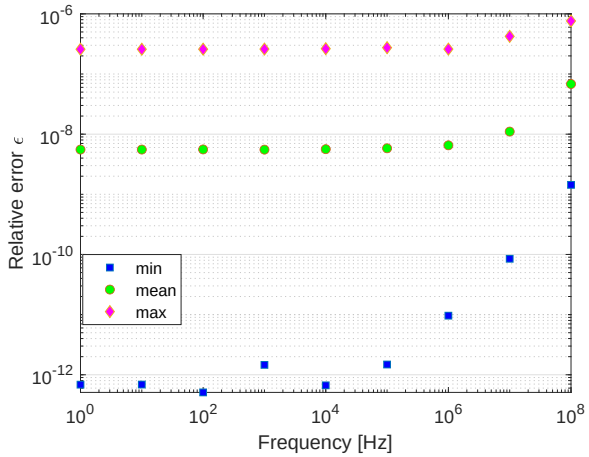

Figure 10: Parallel example in sec. 5.1, for the conductor case. Max, min and mean error values at different frequencies, among the different configurations tested with the adopted mesh.

which result in a rectangle. Table 5 summarizes the total computational time for an increasing numbers of rectangles and, therefore, possible combinations of the patches in the meshes, highlighting the acceleration provided by the proposed approach. Figure 10 shows the max, min and mean error values for 10 frequencies, logarithmic spaced between the 0 and 100 MHz. For the case $d_z \neq 0$, the total number of patches obtained by using formula (66) is equal to 441. For the case $d_z =$, we considered 2 meshes: the first given by the patches below Π (dark blue rectangle), of size (4×6), which gives a total number of possible combinations equal to 210; the second given by the patches on the left of Π (dark blue rectangle), of size (2×4), which gives a total number of possible combinations equal to 30. The total number of combination considered is therefore equal to 441+210+30 = 681. Note that the relative error is undefined when $|I_{ref}| = 0$, and this condition occurs in the megahertz frequency range for conductors, where the error ϵ is not provided, as depicted in Fig. 11 for the real part of the integral. The minimum errors occur for rectangles that do not touch. The largest errors occur for the configurations depicted in Fig. 12 for $d_z = 0$, and different aspect ratio. As expected, the largest errors occur when the kernel of the quadruple integral becomes nearly singular.

5.1.2. Parallel mesh. Dielectric interior problem

In this section, we show the results for the dielectric interior problem. For ideal dielectrics, the phase constant can be considered real and equal to $\beta = \omega\sqrt{\mu_0\mu_r\varepsilon_0\varepsilon_r}$. It is assumed $\varepsilon_r = 4.1$. The computational times are similar to the conductor case. Fig. 13 shows the error for the mesh computed as before, with 681 different combinations, and a total of 10 frequency points that are unequally spaced between 0 and 1 GHz. The real part of the I_{dec} and I_{ref} integrals is depicted in Fig. 14.

5.2. Orthogonal rectangles

In this section, we show the acceleration provided with the proposed formula in eq. (64) for the orthogonal case compared with the standard double-integral formulation in eq. (39). We investigate the relative error for different relevant configurations and aspect ratio, similarly as it was done for the parallel case. We consider a main fixed surface, in the xz-plane, and a mesh in the xy-plane, as depicted in Fig. 16 and 17, and computing the interaction integrals of the main fixed surface (dark blue) with all combinations of the patches in the selected mesh obtained as described for the parallel case.

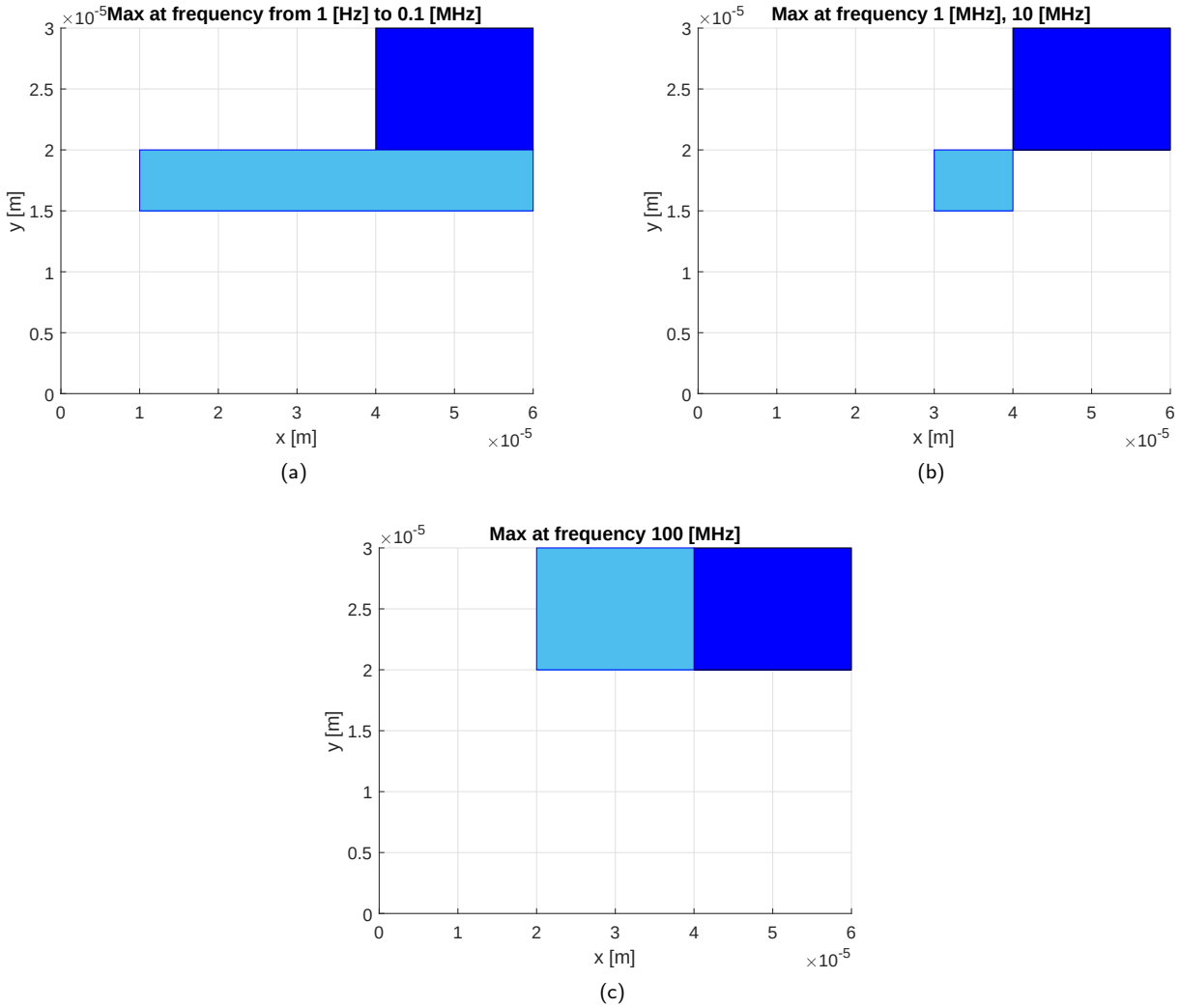

Figure 12: Critical configurations (largest error) in the parallel case, based on the proposed mesh with 681 combinations.

Table 6
Computational time for different orthogonal meshes (conductor case), for 10 logarithmic-spaced frequency points in the interval .

Numb. of configurations	1470	5904	14850
Computational time I_{ref}	60 min	3.5 h	10 h
Computational time I_{dec}	4 min	15.5 min	40 min
Acceleration	× 15	× 13.5	× 15

5.2.1. Orthogonal mesh. Conductor interior problem

The standard integral and the decoupled integral are solved for 10 frequency points, for the meshes depicted in Fig. 16 and 17. The interaction integrals are computed between the main rectangle and the patches plus all possible combinations of them which result in a rectangle. Table 6 summarizes the total computational time for the meshes with an increasing numbers of rectangles and, therefore, possible combinations, highlighting the acceleration provided by the proposed approach. Figure 18 shows the max, min and mean error values for 10 frequencies, logarithmic spaced between the 0 and 1 MHz. The real part of the integral is depicted in Fig. 15. The largest errors occur for the configurations depicted in Fig. 19, between rectangles with a different aspect ratio.

5.2.2. Orthogonal mesh. Dielectric interior problem

As before, it is assumed $\varepsilon_r = 4.1$. The computational times are similar to the conductor case. Fig. 20 shows the error for the mesh with different combinations, and a total of 10 points that are unequally spaced between 0 and 1 GHz. The real part of the integrals is depicted in Fig. 21.

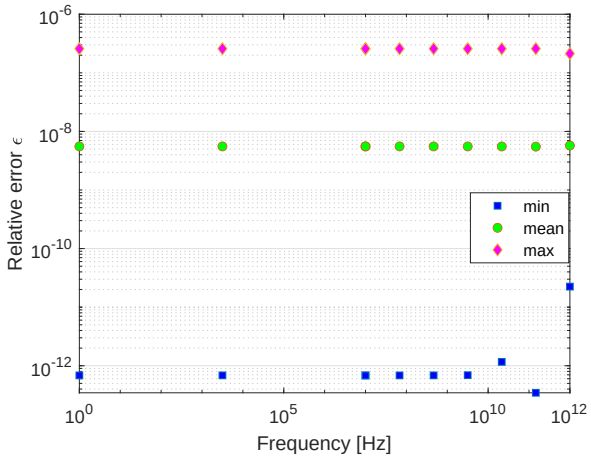

Figure 13: Parallel example in sec. 5.1, dielectric case. Max, min and mean error values at different frequencies, among the different configurations tested with the adopted mesh.

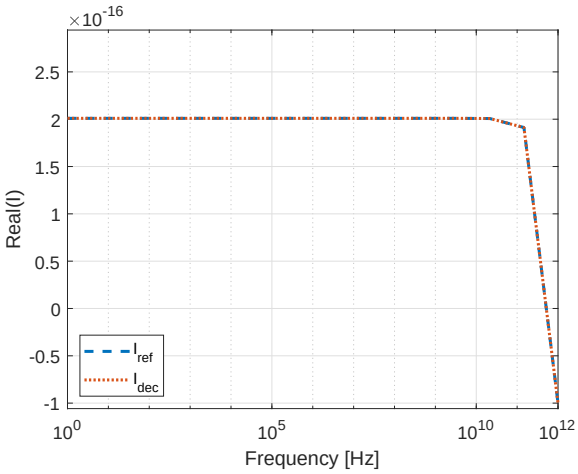

Figure 14: Real part of the integrals for the parallel mesh with 681 combinations, dielectric case.

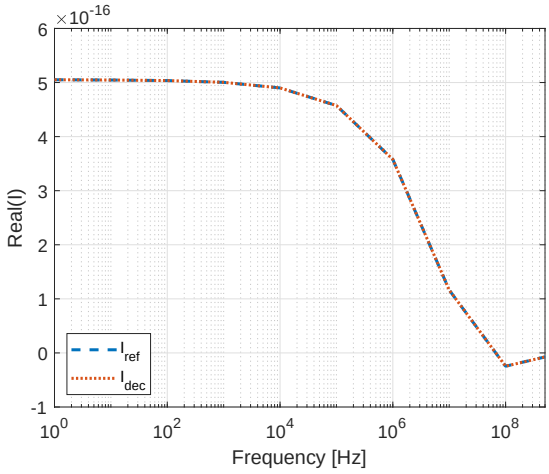

Figure 15: Real part of the integrals for the orthogonal mesh with 1470 combinations, conductor case.

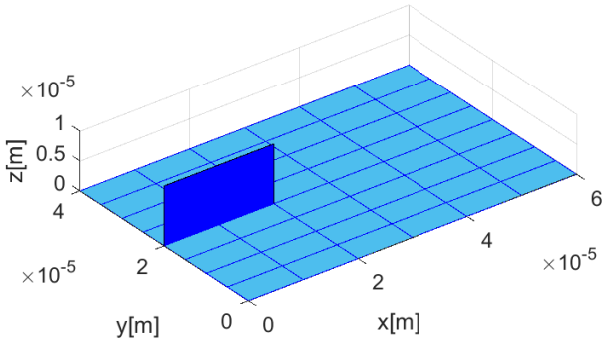

Figure 16: Mesh used to test several combinations in the orthogonal case for potentially touching rectangles.

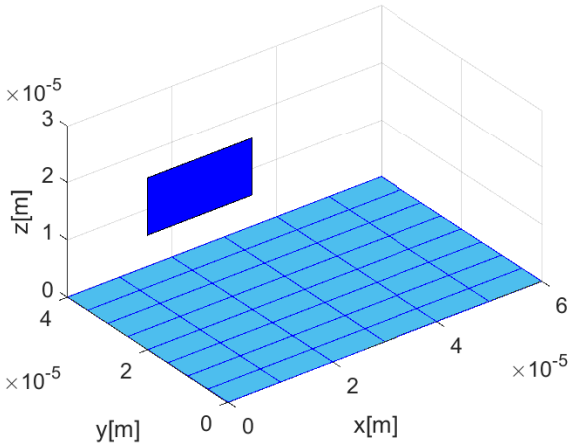

Figure 17: Mesh used to test several combinations in the orthogonal case for rectangles at a distance of 20 µm.

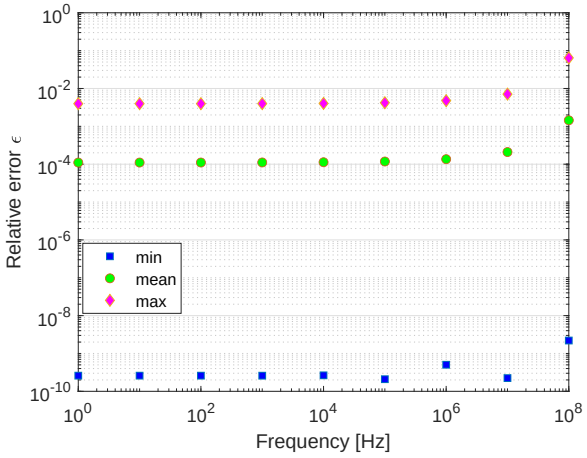

Figure 18: Orthogonal example in sec. 5.2. Max, min and mean error values at different frequencies, among the different configurations tested with the adopted mesh.

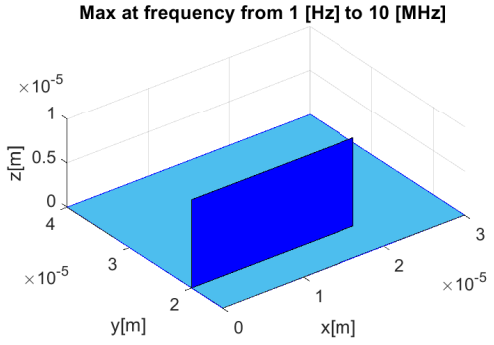

(a)

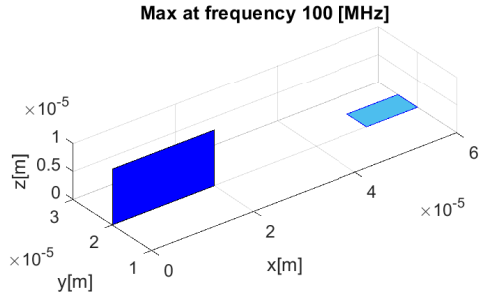

(b)

Figure 19: Critical configurations (largest error) in the orthogonal case, based on the proposed mesh.

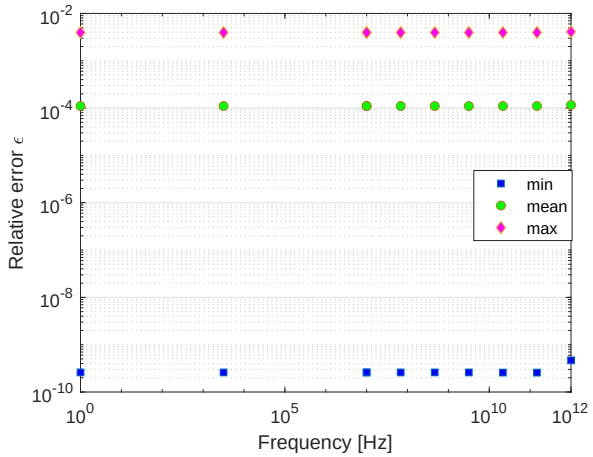

Figure 20: Orthogonal example in sec. 5.1, for the mesh with 1470 combinations, dielectric case. Max, min and mean error values at different frequencies, among the different configurations tested with the adopted mesh.

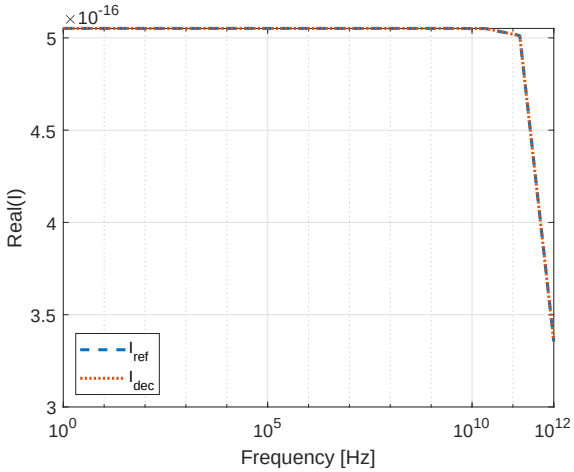

Figure 21: Real part of the integrals for the orthogonal mesh with 1470 combinations, dielectric case.

6. Conclusions

A common strategy to treat the singularities and reduce the computational time of quadruple integrals in CEM problems is to decouple them into low-order integrals. The case of triangular meshes is well-studied in literature because triangular meshes are used in well-known techniques, such as the Method of Moments. However, the most recent S-PEEC method usually adopts a rectangular and orthogonal mesh, which calls for a different type of analysis. Only recently, the work in [30] showed how to decouple a double-surface integral used in the S-PEEC method but only in the 2D scenario, namely for the self-interaction integrals. In this work, we extend and generalize the work to 3D, namely for mutual-interaction integrals. We propose a numerical approach that treats the singularity and, at the same time, reduces the computation complexity of one of the two quadruple integrals used in the S-PEEC method. With the aid of graphical representation, in the parallel case, we show how to decouple the 4D integral into single integrals, and in the orthogonal case, we show how to decouple the 4D integral into single and double integrals. Among the integrals, we provided a closed-form solution only for one; the others are computed numerically. We investigated the computational time and the accuracy of the proposed solution using the available functions in Matlab®. The numerical examples show a remarkable acceleration of the proposed decoupled integral compared to the standard 4D integral while retaining a comparable degree of accuracy. Future work will extend the approach to the integral that involves the curl of Green's function and will investigate the proposed strategy in real-case CEM modeling structures.

References

[1] R. F. Harrington, Field Computation by Moment Methods, Krieger, Malabar, 1982.

[2] A. E. Ruehli, G. Antonini, L. Jiang, Circuit Oriented Electromagnetic Modeling Using the PEEC Techniques, Wiley-IEEE Press, Hoboken, New Jersey, 2017.

[3] C. A. Balanis, Advanced Engineering Electromagnetics, John Wiley & Sons, 2012.

[4] G. Antonini, A. E. Ruehli, Fast multipole and multi-function PEEC methods 2 (4) (2003) 288–298.

[5] G. Antonini, Fast multipole method for time domain PEEC analysis 2 (4) (2003) 275–287.

[6] G. Antonini, A. E. Ruehli, Waveform relaxation time domain solver for subsystem arrays, IEEE Transactions on Advanced Packaging 33 (4) (2010) 760–768. doi:10.1109/TADVP.2010.2061229.

[7] Sheldon X.-D. Tan and Lei He, Advanced Model Order Reduction Techniques in VLSI Design, Cambridge.

[8] R. W. Freund, Krylov-subspace methods for reduced-order modeling in circuit simulation, J. Comput. Appl. Math. 123 (2000) 395–421.

[9] F. Ferranti, M. Nakhla, G. Antonini, T. Dhaene, L. Knockaert, A. Ruehli, Multipoint full-wave model order reduction for delayed PEEC models with large delays, IEEE Transactions on Electromagnetic Compatibility 53 (4) (2011) 959 –967. doi:10.1109/TEMC.2011.2154335.

[10] F. Ferranti, M. Nakhla, G. Antonini, T. Dhaene, L. Knockaert, A. Ruehli, Interpolation-based parameterized model order reduction of delayed systems, IEEE Transactions on Microwave Theory and Techniques 60 (3) (2012) 431 –440. doi:10.1109/TMTT.2011.2181858.

[11] Y. Dou, K.-L. Wu, A passive full-wave micromodeling circuit for packaging and interconnection problems, IEEE Transactions on Microwave Theory and Techniques 67 (6) (2019) 2197–2207. doi:10.1109/TMTT.2019.2909023.

[12] L. Lombardi, Y. Tao, B. Nouri, F. Ferranti, G. Antonini, M. S. Nakhla, Parameterized model order reduction of delayed PEEC circuits, IEEE Transactions on Electromagnetic Compatibility 62 (3) (2020) 859–869. doi:10.1109/TEMC.2019.2919909.

[13] Y. Dou, K.-L. Wu, Nature of antenna radiation revealed by physical circuit model, IEEE Transactions on Antennas and Propagation 69 (1) (2021) 84–96. doi:10.1109/TAP.2020.3008676.

[14] Z. Zhu, B. Song, J. K. White, Algorithms in FastImp: A fast and wide-band impedance extraction program for complicated 3-D geometries, IEEE Transactions on Computer-Aided Design of Integrated Circuits and Systems 24 (7) (2005) 981–998.

[15] D. Gope, A. E. Ruehli, C. Yang, V. Jandhyala, (S) PEEC: Time- and frequency-domain surface formulation for modeling conductors and dielectrics in combined circuit electromagnetic simulations, IEEE Transactions on Microwave Theory and Techniques (6) (2006) 2453–2464.

[16] Y. Jiang, K.-L. Wu, Quasi-static surface-PEEC modeling of electromagnetic problem with finite dielectrics, IEEE Transactions on Microwave Theory and Techniques 67 (2) (2018) 565–576.

[17] E. J. Kansa, J. Geiser, Numerical solution to time-dependent 4D inviscid Burgers' equations, Engineering Analysis with Boundary Elements 37 (3) (2013) 637–645.

[18] D. Latypov, Evaluation of the 4-D singular and near singular potential integrals via the Stokes' theorem, Engineering Analysis with Boundary Elements 125 (2021) 201–207.

[19] P. Yla-Oijala, J. Markkanen, S. Jarvenpaa, S. P. Kiminki, Surface and volume integral equation methods for time-harmonic solutions of Maxwell's equations, Progress in electromagnetics Research 149 (2014) 15–44.

[20] G. Vecchi, Loop-star decomposition of basis functions in the discretization of the EFIE 51 (2) (1999) 339–346.

[21] M. Taskinen, P. Yla-Oijala, Current and charge integral equation formulation, Antennas and Propagation, IEEE Transactions on 54 (1) (2006) 58 – 67. doi:10.1109/TAP.2005.861580.

[22] C. Ho, A. Ruehli, P. Brennan, The modified nodal approach to network analysis 22 (6) (1975) 504–509.

[23] D. Gope, A. Ruehli, V. Jandhyala, Solving low-frequency EM-CKT problems using the PEEC method, IEEE Transactions on Advanced Packaging 30 (2) (2007) 313–320. doi:10.1109/TADVP.2007.896000.

[24] D. Romano, G. Antonini, M. D'Emidio, D. Frigioni, A. Mori, M. Bandinelli, Rigorous DC solution of partial element equivalent circuit models, IEEE Transactions on Circuits and Systems I: Regular Papers 63 (9) (2016) 1499–1510. doi:10.1109/TCSI.2016.2578286.

[25] J. Rivero, F. Vipiana, D. R. Wilton, W. A. Johnson, Evaluation of 4-D reaction integrals via double application of the divergence theorem, IEEE Transactions on Antennas and Propagation 67 (2) (2018) 1131–1142.

[26] D. J. Taylor, Accurate and efficient numerical integration of weakly singular integrals in Galerkin EFIE solutions, IEEE Transactions on Antennas and Propagation 51 (7) (2003) 1630–1637.

[27] J. D'Elía, L. Battaglia, A. Cardona, M. Storti, Full numerical quadrature of weakly singular double surface integrals in Galerkin boundary element methods, International Journal for Numerical Methods in Biomedical Engineering 27 (2) (2011) 314–334.

[28] S. Chakraborty, V. Jandhyala, Evaluation of Green's function integrals in conducting media, IEEE Transactions on Antennas and Propagation 52 (12) (2004) 3357–3363.

[29] F. D. Murro, D. Romano, M. De Lauretis, I. Kovacevic-Badstubner, L. Lombardi, U. Grossner, J. Ekman, F. Frezza, G. Antonini, Efficient computation of partial elements in the full-wave surface-peec method, IEEE Transactions on Electromagnetic Compatibility 63 (4) (2021) 1189–1201. doi:10.1109/TEMC.2021.3052358.

[30] F. Di Murro, J. Ekman, I. Kovačević-Badstübner, U. Grossner, M. Lucido, F. Frezza, D. Romano, G. Antonini, Semi-analytical form of full-wave self-interaction integrals over rectangles, IEEE, 2020 In-

ternational Symposium on Electromagnetic Compatibility-EMC EUROPE, IEEE, 2020, pp. 1–5.
[31] L. F. Shampine, Vectorized adaptive quadrature in MATLAB, Journal of Computational and Applied Mathematics 211 (2) (2008) 131–140.
[32] L. F. Shampine, Matlab program for quadrature in 2d, Applied Mathematics and Computation 202 (1) (2008) 266–274.
[33] M. Hosea, integralN.m, accessed: 2021-08-25.
URL www.mathworks.com/matlabcentral/fileexchange/47919-integraln-m),MATLABCentralFileExchange